6.0 SEISMIC HAZARD ANALYSIS

6.1 Introduction

Following the methodology of the DCPP Long Term Seismic Program, the seismic hazard is evaluated using both deterministic seismic hazard analysis (DSHA) and probabilistic seismic hazard analysis (PSHA) approaches.

It is important to keep in mind that the source characterizations in Section 5 and the analysis of logic trees to produce seismic hazard results in Section 6 involve using the elements of the source characterizations and logic trees in a mathematical model. The elements of the model are simplified representations of more complex faults or fault zones identified in the DCPP vicinity based on geological, geophysical, and seismological measurements and observations. In Section 5 and continuing in this section, the terminology that is used distinguishes the modeled elements as "fault sources" and the real-Earth features as "fault zones". For example, the Shoreline fault source is the model representation for the Shoreline fault zone, and the San Luis Bay East segment source is the model for the San Luis Bay East fault segment. The mathematical models are simplifications of the real world.

The source characterization described in Section 5 provides descriptions of the alternative geometries, senses of slip, and slip rates of the main fault sources in the DCPP region. Additional source characterization parameters are required for the DHSA and PSHA: the mean characteristic magnitude and the magnitude probability density function. These additional parameters are described in Sections 6.3 and 6.4.

The logic trees in Section 5 include several correlations between the four main fault sources: Shoreline, San Luis Bay, Los Osos, and Hosgri. As a result of these correlations, the full logic tree becomes very large and a simplification is needed for application to the DSHA and PSHA. The simplifications made to the logic trees are described in Section 6.2

The DCPP site conditions are described in Section 6.5 and ground motion models are described in Section 6.6. The results of the DSHA and PSHA are described in Sections 6.7 and 6.8, respectively.

6.2 Simplified Logic Trees

As described in the Section 5, the logic trees for the Shoreline and San Luis Bay fault sources are correlated through the “linked” branch (branch 12 on Figure 5-3). There are additional correlations between the other fault sources. The logic trees for the San Luis Bay and Los Osos fault sources are correlated because the San Luis Bay fault source is truncated at depth by the intersection with the Los Osos fault source (note 3 on Figure 5-5). The depth at which the Los Osos and San Luis Bay fault sources intersect depends on the depths and dips of the two fault sources. The logic trees for the Shoreline and San Luis Bay fault sources are also correlated to the logic tree for the Hosgri fault source because the San Luis Bay West segment source and Shoreline North segment source are truncated at depth by the intersection with the Hosgri fault source (note 3 on Figure 5-11 and note 2 on Figure 5-3). These truncations depend on depth to the bottom of the fault source and the dips of the three fault sources. Using the logic trees as described in Section 5 leads to over 60,000,000 alternative for the rupture geometries and slip rates of the Shoreline fault source. To reduce the logic tree for the Shoreline fault source to a

manageable size, simplifications to the logic trees for the Los Osos, San Luis Bay, and Shoreline fault sources are made. The simplifications are described below.

6.2.1 Shoreline Fault Source

In the Shoreline fault source logic tree, the northern end of the North segment is truncated by the Hosgri fault source (Note 2 on Figure 5-3). This truncation is ignored and the Shoreline fault North segment source is allowed to cross the Hosgri fault source. The amount of overlap is small and will have a negligible effect on the fault source area and hazard.

For the linked case, the rupture from the Shoreline Central segment source onto the San Luis Bay East segment source has three alternative end points for the east end (Note 4, Figure 5-6). A single model in which the full length of the East segment source is used replaces these three alternatives.

For the linked case, the slip rate of the South segment source is reduced by the slip rate of the San Luis Bay East segment source (Note 8, Figure 5-6). This adds additional correlation between the San Luis Bay and Shoreline logic trees. As a simplification, a mean slip rate of 0.18 mm/yr for the San Luis Bay East segment source is removed from the South segment (linked branch only) with the constraint that the slip rate on the South segment is not less than 0.05 mm/yr.

6.2.2. San Luis Bay Fault Source

In the linked model for the Shoreline and San Luis Bay fault source logic tree (Figure 5-5), the western end of the San Luis Bay West segment source is truncated by the Hosgri fault source (Note 2 on Figure 5-5). This truncation is ignored, and the San Luis Bay West segment source is modeled as crossing the Hosgri fault source. The amount of overlap is small and will have a negligible effect on the fault source area and hazard.

In the linked model, the San Luis Bay East segment source has two alternative dips (80 and 85 degrees), is truncated by the Los Osos fault source, and has three alternative senses of slip. For linked ruptures that include the San Luis Bay East and the Shoreline Central segment sources, three simplifications are made to the logic tree. First, the dip of the San Luis Bay East segment source is modeled as 90 degrees (consistent with dip of the Shoreline fault source). The difference in the down dip fault source width for a dip of 80 degrees as compared to a dip of 90 degrees is less than 1.5 percent. Second, the truncation of the San Luis Bay East segment source by the Los Osos fault source is ignored. The logic tree models the Shoreline Central segment source as crossing the Los Osos fault source, so this simplification leads to a consistent model for the linked ruptures. Third, the sense of slip for the linked fault sources is modeled as strike-slip. The linked rupture has a mixture of strike slip on the Shoreline Central segment and reverse, reverse-oblique, or strike slip on the San Luis Bay East segment source. The ground motion models require a single sense of slip for an individual earthquake. Given that the Shoreline Central segment source is closest to the DCPP and has a weight of 1.0 for strike-slip faulting, the strike-slip sense of slip is applied to all linked ruptures, because the ground motions are most influenced by the closest portion of the rupture to the site.

In the linked model, there are also separate ruptures of the San Luis Bay East segment source by itself. For these single-segment-source ruptures, the logic tree is simplified to use a single dip of

83 degrees in place of the two values of 80 and 85 degrees. The truncation of the San Luis Bay East segment source by the Los Osos fault source is included, but the correlation with the dip of the Los Osos fault is not modeled. As this segment source has a small contribution to the hazard, ignoring the correlation will not have a significant effect on the fractiles (epistemic uncertainty) of the hazard.

6.2.3 Los Osos Fault Source

The Los Osos logic tree includes alternative for the east end of the fault (branch 1 on Figure 5-10). In the simplified model, the longer fault length (57 km) is used with a weight of 1.0. This simplification leads to a slightly larger fault source, but because the rupture lengths are fixed in branch (Figure 5-10) at 19 km and 36 km, this simplification has no effect on the deterministic analysis and only a small increase in the hazard for the probabilistic analysis.

6.2.4 Simplified Logic Tree for the Shoreline Fault Source

With the simplifications noted above, the total number of alternative models for the rupture geometries and slip rates of the Shoreline fault source is reduced to about 500,000. The simplified parts of the logic trees for the Shoreline fault source are shown on Figures 6-1 and 6-2.

The coordinates of the top edges of the fault segment sources are listed in Table 6-1a. The geometry of the San Luis Bay West segment source is more complicated due to the truncation by the Shoreline fault source. For simplicity, the west end of the intersection with the Shoreline fault was fixed at Shoreline fault coordinate S2 (Figure 5-1). The coordinates used for alternative models of the San Luis Bay West segment source are listed in Table 6-1b.

The depth of intersections of the San Luis Bay Fault source with the Los Osos Fault source are listed in Table 6-2a for the not-linked branch and in Table 6-2b for the linked branch.

6.3 Mean Characteristic Magnitude Models

For fault sources, the mean characteristic magnitude is estimated using the Wells and Coppersmith (1994) (WC) and Hanks and Bakun (2008) (HB) models. These models are listed in Table 6-3.

For the Hosgri and Shoreline fault sources, which are strike-slip, the HB model and HC strike-slip (SS) model are used with weights of 0.7 (HB) and 0.3 (WC). The HB model is preferred because it does a better job of capturing the magnitude-area scaling for large strike-slip earthquakes in California (Hanks and Bakun, 2008). For the Los Osos and San Luis Bay fault sources, which are reverse (RV) and reverse-oblique (RV/OBL), the Wells and Coppersmith "All Fault Type" (ALL) model is used with a weight of 1.0.

The epistemic uncertainty in the mean magnitude is estimated from the standard error of the estimated coefficients given by Wells and Coppersmith (1994) and shown in Table 6-3. For strike-slip earthquakes, the standard error of 0.07 is used. For the reverse and reverse-oblique earthquakes, the average of the standard errors of the ALL model and the RV model is used (0.09). These standard errors are estimates of the epistemic uncertainty of the constant term for a

single model. Because two strike-slip models are used, the standard error of 0.07 for strike-slip earthquakes is reduced by 1/SQRT(2), leading to a standard error of the mean of 0.05.

For the logic tree, a three-point distribution is used with values of –1.6 σ, 0 σ, and 1.6 σ with weights of 0.2, 0.6, and 0.2, respectively, where σ is the standard error of the mean. For strike-slip earthquakes, this corresponds to ±0.08 magnitude units. For reverse and reverse-oblique earthquakes, this corresponds to ±0.15 magnitude units.

6.4 Magnitude Probability Density Function

The two main classes of magnitude probability density functions (pdfs) used in probabilistic seismic hazard analyses (PSHAs) are truncated exponential models and characteristic earthquake models. There are several different forms of the characteristic earthquake model, but the main feature is that the characteristic model has a higher pdf near the characteristic magnitude than the exponential model. The truncated exponential model has long been known to work well for large regions, but for individual faults, the characteristic model is preferred in most PSHA applications.

The primary reason usually given for using the characteristic model is that the truncated exponential model greatly overpredicts (by about a factor of 5) the rate of small earthquakes that occur along a fault if the maximum magnitude is determined following standard practice (e.g. based on the area of the fault) and the activity rate of a fault is typically estimated by balancing the accumulation and release of seismic moment (e.g. Geomatrix, 1993). This conclusion depends on the horizontal width of the zone around the fault that is used to determine which earthquakes occur on the fault. If wide zones (e.g. ±20 km) around the fault are included, then the fault zones become regions and the exponential distribution is applicable.

The overprediction of small magnitude earthquakes by the exponential model can be avoided by increasing the maximum magnitude about 1.5 units above the mean magnitude computed from magnitude-area scaling relations. To test the exponential model with the large maximum magnitude model, the observed distribution surface slip at a point from multiple earthquakes can be used. Hecker et al. (2010) compiled a set of paleoseismic observations of slip at sites with more than one earthquake and found that the coefficient of variation (CV) is about 0.4.

Using the Wells and Coppersmith (1994) model for average displacement with a uniform distribution of magnitudes (M 6–8) and including the effects of variability of slip along strike, the CV for the exponential model with large maximum magnitudes is about 1.0 which is much larger than the observed CV of 0.4, indicating that the exponential distribution can be rejected for use for individual faults. Some form of characteristic model should be used for individual faults.

In this report, the composite model (mixture of characteristic earthquakes with an exponential tail at smaller magnitudes) is used for the magnitude pdf for all fault sources. The most commonly used composite model is the Youngs and Coppersmith (1985) model. The form of the Youngs and Coppersmith model is shown on Figure 6-3. The model corresponds to approximately 94 percent of the seismic moment being released in characteristic and 6 percent of the moment being released in the exponential tail. Using this model, the CV for slip at a point is

about 0.6, which is still larger than the observed CV of 0.4, but is much closer than the exponential model. Therefore, the composite model is adopted for individual faults.

To address the epistemic uncertainty of the composite model, the fraction of the moment that is released in characteristic earthquakes was varied in a sensitivity study using 90, 94, and 97 percent (Figure 6-3) with weights of 0.2, 0.6, and 0.2, respectively. Changing this parameter mainly affects the rate of earthquakes in the exponential tail of the distribution. The results of the sensitivity study showed that including this epistemic uncertainty changed the mean hazard by about 1 percent and changed the 10th and 90th fractiles by about 3 percent. The effect is small because the hazard at DCPP is dominated by the characteristic earthquakes. Due to the small effect, the epistemic uncertainty in the magnitude pdf is ignored and the Youngs and Coppersmith (1985) model is used with a weight of 1.0.

6.5 Site Condition

The ground motion models described in Section 6.6 use the shear-wave velocity in the top 30 m as the site parameter. This parameter, called V_{S30}, was computed for the DCPP power block using a shear-wave profile measured at the power block location in 1978 (PG&E, 1988). The estimated V_{S30} for the rock under the power block foundation is 1,200 m/s (GEO.DCPP.10.01).

The methods for measuring shear-wave velocity have improved significantly since 1978. New measurements of the shear-wave velocity profile were made at the DCPP ISFSI site as part of the ISFSI site characterization (PG&E, 2004). Because the ISFSI is located on the same geologic unit as the power block, the recent shear-wave velocity measurements for the DCPP ISFSI are used to compute the V_{S30} at the ISFSI location for comparing with the results based on the older shear-wave velocity measurements.

The V_{S30} values are listed in Table 6-4. For the measurements at the ISFSI site, the V_{S30} was measured without the top 10 m to be consistent with the embedment depth of the power block foundation. The V_{S30} values for the ISFSI are very similar to the V_{S30} based on the 1978 data. The estimate of V_{S30}=1200 m/s for the power block foundation remains applicable.

6.6 Ground Motion Prediction Equations

The Next Generation Attenuation (NGA) models represent the current state-of-practice for estimating ground motions from crustal earthquakes in active tectonic regions. The five NGA ground motion prediction equations (GMPEs) for the average horizontal component are used: Abrahamson and Silva, 2008 (AS08); Boore and Atkinson, 2008 (BA08); Campbell and Bozorgnia, 2008 (CB08); Chiou and Youngs, 2008(CY08); and Idriss, 2008 (I08).

Four of the NGA GMPEs use V_{S30} for the site classification parameter. The fifth model, that of Idriss (2008), does not use V_{S30} directly, but rather it is uses two V_{S30} ranges: 450–900 m/s and > 900 m/s. Three of the NGA models include an additional site parameter based on the depth to rock. The AS08 and CY08 models use depth to V_S=1.0 km/sec ($Z_{1.0}$), and the CB08 model uses the depth to V_S=2.5 km/sec ($Z_{2.5}$).

The five GMPE models were given equal weights for the analysis. Recent studies (EPRI, 2006; PG&E 2010c) have shown that there is no statistical basis for truncating the lognormal

distribution at less than three standard deviations, but that there must be some upper limit to the ground motion based on physical limits. Therefore, a truncation of the lognormal distribution at 4 standard deviations is applied to all of the GMPEs.

6.6.1 Epistemic Uncertainty

In the past, it has been standard practice to address epistemic uncertainty in ground motion estimation by using a weighted set of applicable models under the assumption that the alternative models were developed somewhat independently, and thus capture the uncertainty in the estimation of ground motions; however, the NGA set of ground motion models were developed as part of a collaborative effort with many interactions and exchange of ideas among the developers. Therefore, the need for additional epistemic uncertainty should be considered when applying the set of NGA models. Although the models are based on the same initial data set, the NGA models differ in the subset of data used and in their functional forms. As a result, there is considerable variability in the ground motion estimates for conditions that are not well represented in the empirical data, such as on the hanging wall of dipping faults, as described in the following subsections.

Variability Among PEER-NGA Models

Youngs (2009) evaluated the differences in the median ground motions given by the NGA models for a range of source/site geometries in terms of the standard deviation of the medians for the four NGA models that use V_{S30} as a site parameter. Youngs (2009) found that, for strike-slip earthquakes, the standard deviation is larger for **M** 5.5 than for **M** 6.5 and **M** 7.5, reflecting both the small number of small magnitude events in the NGA data set and the different modeling of the depth-to-top-of-rupture scaling in the NGA models. Youngs (2009) also found that there tend to be larger standard deviations for reverse faults in the hanging wall region (R_x<20 km) for large-magnitude earthquakes, which reflects the much smaller amount of data in the NGA data set for this condition and the differences between the NGA models in the treatment of ground motions on the hanging wall.

Epistemic Uncertainty in a Single NGA Model

One approach for assessing the level of the additional epistemic uncertainty is to evaluate how well the empirical data constrain the NGA models. The U.S. Geological Survey (Petersen et al., 2008), following initial suggestions by the NGA developers, adopted the simple approach of using the square root of the sample size in specific magnitude and distance bins to define the relative epistemic uncertainty in an individual NGA ground motion model as a function of magnitude and distance; however, this approach ignores the fact that the constraints on model predictions are not based solely on the data in any one magnitude and distance interval.

Youngs (2009) used an alternative approach to estimating the epistemic uncertainty of the median for any one NGA model based on the statistics of the model fit combined with the data distribution to compute standard errors of the median estimates as a function of magnitude and distance. The asymptotic standard errors in the median ground motion were computed using this approach for the Chiou and Youngs (2008) NGA model. For strike-slip earthquakes, the epistemic uncertainty is between 0.1 and 0.18 natural log units. For reverse and normal earthquakes, the epistemic uncertainty at large distance is similar to the epistemic uncertainty for strike-slip earthquakes (0.1 to 0.18), but increases to up to 0.3 at short distances on the hanging

wall. As is shown below (Figure 6-4a), this increase in the uncertainty at short distances for dipping faults is covered by the range in the five NGA models.

For this report, a simple model of the additional epistemic uncertainty of the median is developed. The Youngs (2009) model provides the estimates of the epistemic uncertainty of a single model due to data base limitations. The five NGA models provide some or all of this range depending on the magnitude, distance, and style of faulting. For the fault sources important to hazard at DCPP, the median ground motions from each of the five NGA models are computed. The epistemic uncertainty captured by the distribution of the five NGA models is measured by the standard deviation of the median ground. This is epistemic uncertainty is then compared to the Youngs (2009) uncertainty. If the standard deviation of the NGA models is less than the epistemic uncertainty from Youngs (2009), then additional epistemic uncertainty is added. The need for additional epistemic uncertainty was evaluated separately for the four nearby faults sources.

For each fault source, the range of the median ground motions from the five NGA models is evaluated for representative scenario earthquakes. The magnitude of the representative scenario is taken as the median (50th fractile) of the mean characteristic earthquake (see Section 6.7.1) and distance is the taken as the closest distance to the site. The representative scenario earthquakes are M=6.8 for the Hosgri, M=6.5 for the Los Osos, M=6.1 for the San Luis Bay, and M=6.2 for the Shoreline. The standard deviations of the median ground motions for each of the representative scenarios earthquakes are shown on Figure 6-4a. These standard deviations of the medians are compared to the Youngs (2009) minimum epistemic uncertainty in this figure. For sites located on the hanging wall for reverse earthquakes, there is a large range of the median ground motions in the NGA models, whereas, for sites located close to large strike-slip earthquakes, the range of the median ground motions is much smaller.

The additional epistemic uncertainty required to reach the Youngs (2009) standard deviations is shown on Figure 6-4b. The key frequency range for DCPP is in the intermediate frequency range (3–8.5 Hz). In this range, the additional epistemic uncertainty required for the four scenarios separates into two groups: the Shoreline, San Luis Bay, and Los Osos fault sources require a small additional epistemic uncertainty; the Hosgri fault source requires a large additional epistemic uncertainty. For simplicity, smoothed models of the additional epistemic uncertainty were developed for these two groups as shown on Figure 6-4b.

Epistemic Uncertainty Model

The epistemic uncertainty in the median NGA models is modeled using a three-point discrete approximation to a normal distribution. This approach places a weight of 0.6 on the median model and weights of 0.2 on the 5th and 95th percentiles (±1.6 standard deviations). This approach is implemented by developing three alternative models for each NGA relationship: one model equal to the original relationship, and two models with $\pm 1.6\sigma_E$ added to the constant term, each with weight 0.2. A smoothed model of the period dependence of the epistemic factor, F_E, for the Hosgri fault is given in Eq. (6-1):

$$F_E = \begin{cases} 0.20 & for\ T \le 1.0 \\ 0.20 + 0.20\left(\dfrac{T-1}{4}\right) & for\ 1.0 < T < 5.0 \\ 0.40 & for\ T \ge 5.0 \end{cases} \quad (6\text{-}1)$$

The smoothed model for the period dependence of the epistemic factor for the San Luis Bay, Shoreline, and Los Osos faults is given in Eq. (6-2):

$$F_E = \begin{cases} 0.10 & for\ T \le 1.0 \\ 0.10 + 0.20\left(\dfrac{T-1}{4}\right) & for\ 1.0 < T < 5.0 \\ 0.30 & for\ T \ge 5.0 \end{cases} \quad (6\text{-}2)$$

The logic tree for the median ground motion is shown on Figure 6-5.

6.6.2 Hard-Rock Site Effects

As described in Section 6.5, the DCPP power block foundation has a V_{S30}=1200 m/s which corresponds to a hard-rock site. Although the NGA models can be used for this type of hard-rock site, a V_{S30} of 1200 m/s is outside of the range of V_{S30} that is well constrained by the empirical data used to derive the NGA models. To address this hard-rock condition, an alternative approach is considered using the NGA models to estimate the ground motion for V_{S30}=760 m/s for which they are well constrained. Amplification factors based on generic site response analyses for hard-rock sites are used to scale the V_{S30}=760 ground motions to the DCPP hard-rock conditions.

As part of the PEER NGA project, Silva (2008) developed a suite of amplification factors for a range of generic site conditions based on kappa in the range of 0.038–0.04 seconds for rock sites. Kappa is an empirically derived site parameter that is usually interpreted as a measure of the amount of damping in the rock beneath a site (the Fourier spectrum is scaled by exp(-πkf), where f is frequency). Silva (2008) provides amplification factors relative to a V_{S30}=1100 m/s for 64 cases with different velocity profiles including rock profiles. For this application, two cases are relevant: Case 61 provides amplification factors for V_{S30}=760 m/s for a depth to rock ranging from 9 to 55 m (30 to 180 ft) and Case 64 provides amplification factors for hard rock with V_{S30}=3150 m/s. A comparison of the amplification for these two cases shows that the site amplification is close to linear. Therefore, the amplification from V_{S30}=760 m/s to V_{S30}=1100 m/s can be used to extrapolate to V_{S30}=1200 m/s. The raw and smoothed values of the log amplification, $a_1(T)$, are shown on Figure 6-6 and the smoothed values are listed in Table 6-5.

A key issue related to the use these generic amplification factors for hard-rock sites is the impact of the site-specific kappa value. For generic soft-rock sites in California used in the NGA data sets, the kappa value is about 0.04 seconds (Silva, 2008). For hard-rock sites, the kappa values can be much smaller (kappa values of 0.01–0.02 seconds) leading to an increase in the high frequency content of the ground motions for hard-rock sites.

For DCPP, the site-specific kappa was estimated based on DCPP free-field recordings from the 2003 Deer Canyon earthquake (Appendix L). The recordings from the Deer Canyon earthquake are well suited for evaluating kappa because they are rich in high frequency content due to the short distance to the fault and the small magnitude of the earthquake (high corner frequency). The analysis of the DCPP free-field ground motions from the Deer Canyon earthquake showed that the kappa at DCPP is 0.042 seconds, consistent with typical soft-rock sites in California (Figure 6-7). The relatively high kappa value for the hard-rock DCPP site is interpreted to be due to fractures in the bedrock in the Franciscan. Given this kappa value, the V_{S30} dependence of the site amplification developed by Silva (2008) for a kappa of 0.04 sec can be applied to DCPP without requiring an additional modification for kappa. Using this approach, the site-specific effects of V_{S30} and kappa at the DCPP site are incorporated in the ground motion model rather than extrapolating the NGA models to high V_{S30} values.

Applying these amplification factors, the ground motion for V_{S30}=1200 m/s is computed using the following equation:

$$SA_{1200}(T) = SA_{760}(T)\exp(a_1(T)) \tag{6-3}$$

where $Sa_{760}(T)$ is the median spectrum from the NGA model and $a_1(T)$ is the amplification term listed in the third column of Table 6-5. An example of the effect of using the site-specific method in place of the V_{S30} scaling in the NGA models is shown on Figure 6-8 for an M=7.1, strike-slip earthquake at a distance of 4.9 km. The ground motions based on using V_{S30}=1200 m/s directly into the NGA models are shown by the dashed lines on Figure 6-8, and the ground motions computed using the eq. (6-3) are shown by the solid lines. Using the site-specific approach (solid lines) leads to a narrower range of the ground motion than extrapolating the V_{S30} scaling (dashed lines), indicating the site-specific method is more robust than using extrapolating the V_{S30} scaling in the NGA models.

6.6.3 Average Spectral Acceleration from 3–8.5 Hz

The DCPP fragilities used in the probabilistic risk analyses are based on the average spectral acceleration from 3 to 8.5 Hz. The NGA models, as published, only provide for spectral acceleration at single frequencies. To estimate the 3-8.5 Hz spectral acceleration using the NGA models, the 5 Hz spectral values are computed and then adjustment terms are applied to scale the 5 Hz spectral values to estimate the 3–8.5 Hz spectral accelerations.

The factors to adjust the 5 Hz spectral acceleration to the 3–8.5 Hz spectral acceleration are derived from the NGA data base (Chiou et al., 2008). Using the NGA data for M≥6, rupture distance≤20 km, and V_{S30}≥450 m/s, the average difference between the ln(Sa(5 Hz)) and the ln(Sa(3–8.5hz)) is 0.04 with the 3–8.5 Hz values being slightly lower. In addition to the change in the median value, the use of the spectral acceleration averaged over a frequency band also results in a reduction of the standard deviation. Using the same subset of the NGA data, the variance for the 3–8.5 Hz value is 0.058 lower than the variance for the 5 Hz value.

6.6.4 Single-Station Sigma and Site-Specific Site Effects

Empirical GMPEs describe both the median and the standard deviation of the ground motion. In most empirical ground motion models, the standard deviation is computed from data sets that include recordings at a broad range of sites and from earthquakes located in different regions. By using the observed standard deviation from global models in a seismic hazard analysis, there is an assumption that the variability seen in typical strong motion data sets containing recordings at multiple sites from earthquakes in multiple regions will be the same as the variability seen in the ground motion at a single site from multiple future earthquakes at a single location. This is referred to as the ergodic assumption (Anderson and Brune, 1999).

If recordings at a single site from multiple earthquakes are available, then the variability of the ground motion will be smaller than the variability from typical empirical GMPEs based on global data because the global GMPEs include the effects of variability due to different site conditions that are systematic and repeatable for a single site.

Several recent studies have estimated the reduction in the standard deviation for single sites: Chen and Tsai (2002), Atkinson (2006), Anderson (2010), and Lin et al. (2010). These studies have found that the aleatory variability of ln(PGA) can be reduced by about 10–15 percent for single sites. This reduced standard deviation is called "single-station sigma."

Using the NGA data extended to small magnitudes (Chiou et al, 2010), a preliminary model for the single-station sigma, σ_{SS}, was derived for the NGA models (BCHydro, 2010):

$$\sigma_{SS}(T,M) = (0.87 + 0.0037 \ln(T)) \, \sigma(T,M) \qquad (6\text{-}4)$$

where $\sigma(T,M)$ is the standard deviation given by the NGA models. For PGA, the value at T=0.01 sec is used. Following the notation of Al-Atik et al. (2010), the total standard deviation, σ, can be separated into the single-station sigma and the site-to-site sigma:

$$\sigma(T,M) = \sqrt{\sigma_{SS}^2(T,M) + \sigma_{S2S}^2(T)} \qquad (6\text{-}5)$$

The $\sigma_{S2S}^2(T)$ term, called the site-to-site uncertainty, is the variance of the epistemic uncertainty due to systematic differences in the site amplification between sites with the same V_{S30}.

The single-station sigma approach was first proposed by Atkinson (2006). Its implementation is rapidly developing and is gaining broad acceptance. Two ongoing major projects to update ground motion models in the United States have adopted the single-station sigma approach. The update of the NGA models applicable to the western United States (NGA-west2), being conducted through the Pacific Earthquake Engineering Research Center (PEER, 2010a), will provide single-station sigma values as well as the traditional ergodic sigma values. Similarly, the NGA-east project, sponsored by the NRC and also being conducted through the PEER center (PEER, 2010b), has also adopted the single-station sigma approach.

For the use of the single-station sigma approach, estimates of the median site-specific factor and its epistemic uncertainty are needed (e.g., how does the site-specific site amplification differ

from the global average model for the given V_{S30}?). Observations from earthquakes at the site can be used to constrain the site-specific effects. At DCPP, there are observations of past earthquakes that allow estimates of the site-specific site amplification to be made. These allow the development of GMPEs that are calibrated to the site-specific effects at DCPP.

To use ground motion data recorded at the site in a single-station sigma approach, the within-event residuals need to be computed (Al-Atik et al., 2010) to avoid source-specific effects being mixed in with the site-specific effects. To allow the event term to be reliably estimated requires earthquakes with recordings at multiple sites (5 or more). For DCPP, there are recordings from two recent earthquakes that meet this requirement: the 2003 San Simeon and 2004 Parkfield earthquakes.

The ground motion data and metadata from these two earthquakes are part of the NGA-west2 database (PEER, 2010a). The distribution of the data from these two earthquakes in terms of rupture distance and V_{S30} is shown on Figure 6-9. Most of the data are for $V_{S30} < 450$ m/s so there is not enough data to use with Idriss model which is only for sites with $V_{S30} > 450$ m/s. For the other four NGA models, the total residuals were computed for each earthquake. These total residuals are used to estimate the event terms as described below.

For the San Simeon earthquake, the residuals for 5 Hz and 1 Hz for each NGA model are shown on Figures 6-10a and 6-10b. The rupture distance for the DCPP site is 35 km. The residuals show a slope with distance for large distances. The average residual from sites at distances of 0–100 km is used as the event term representative of mean residual at 35 km. This average residual is shown by the horizontal lines on Figures 6-10a and 6-10b.

For the Parkfield earthquake, the residuals for 5 Hz and 1 Hz for each NGA model are shown on Figures 6-11a and 6-11b. The rupture distance for the DCPP site is 85 km. Again, the residuals show a slope with distance for large distances. The average residual from sites at distances of 40–170 km is used as the event term representative of mean residual at 85 km. This average residual is shown by the horizontal lines on Figures 6-11a and 6-11b.

This process was repeated for the suite of spectral frequencies. The resulting event terms are given in Table 6-6 for the four NGA models.

Next, the event term adjusted median ground motions for the DCPP site are computed using each of the four NGA models for V_{S30}=760 m/s, and the ground motions are then scaled to the V_{S30} for the free-field site condition. The free-field site at DCPP has a V_{S30}=1100 m/s as compared to the V_{S30}=1200 m/s for the embedded power block. Using the same method as described in Section 6.6.2, the Silva (2008) amplification factors are applied to account for the scaling from V_{S30}=760 to V_{S30}=1100 m/s. These factors are listed in Table 6-5.

The median spectra for the free-field site, including the event terms, are shown for the four NGA models on Figures 6-12 and 6-13 for the San Simeon and Parkfield earthquakes, respectively. The small range of the NGA models is a result of applying the model-specific event terms. The average of the event-term adjusted median ground motions is shown by the black lines in Figures 6-12 and 6-13.

Figure 6-14 shows the residuals of the observed free-field ground motion at DCPP computed relative to the event-term corrected NGA median spectrum. The two earthquakes show a consistent trend in the residuals with negative residuals in the 5-10 Hz range and positive residuals in the 0.5-3 Hz range. A smoothed model of the mean residual is also shown in Figure 6-14. The mean residual represents the systematic differences in the site amplification effects at the DCPP site as compared to the average for sites with the same V_{S30} and kappa. (Kappa is included as a known parameter for DCPP because the site amplification model from V_{S30}=760 m/s to V_{S30}=1100 m/s included the effects of a known kappa.) The values of the smoothed mean residuals, called a_2, are listed in Table 6-7.

The a_2(T) site terms represent the site-specific amplification observed at the DCPP site. The site terms show that the DCPP site has increased amplification of low frequency ground motions and reduced amplification of high frequency ground motions as compared to average sites with the same V_{S30} and kappa.

The consistency of the results for the San Simeon and Parkfield earthquakes indicates that this site-specific site amplification is a robust feature, but it is based on only two earthquakes. The uncertainty of the estimate of the mean has a variance of $\frac{\sigma^2_{S2S}(T)}{N}$ where N is the number of observations. Given two earthquakes recorded at the site, N=2, and the epistemic uncertainty in the a_2 values has a variance of $\frac{\sigma^2_{S2S}(T)}{2}$.

For ease of application, this additional epistemic uncertainty is combined with the single-station aleatory variability to provide an equivalent total standard deviation for use in computing the ground motion hazard at the DCPP site. This is a common simplification used in PSHA which yields the correct mean hazard, but the median fractile is biased high and the range of the fractiles is reduced.

From eq. (6-6), the standard deviation of the site-to-site uncertainty is given by:

$$\sigma_{S2S}(T,M) = \sqrt{\sigma^2(T,M) - \sigma^2_{SS}(T,M)} \qquad (6\text{-}6)$$

Three of the five NGA models include a magnitude-dependent standard deviation. To capture standard deviation for the magnitudes relevant for the DCPP site, the standard deviation of the site-to-site uncertainty is averaged over M6, M6.5, and M7. The σ_{S2S} term is then averaged over the five NGA models. The site-to-site variance, $\sigma^2_{SS}(T,M)$, is listed in Table 6-7.

The equivalent total standard deviation is given by

$$\sigma_{EQTotal}(T,M) = \sqrt{\sigma^2(T,M) - \left(1 - \frac{1}{N}\right)\sigma^2_{S2S}(T,M)} \qquad (6\text{-}7)$$

The term $-\left(1-\frac{1}{N}\right)\sigma_{S2S}^2(T,M)$ in eq. (6-7) is the adjustment to the variance given by the NGA models. These variance adjustment terms, for N=2, are listed in the last column of Table 6-7.

The estimation of the median and standard deviation of the ground motion using the single-station approach is summarized as follows. For 5 percent damped spectral acceleration at a single frequency, the median is given by

$$\ln\left(SA_{DCPP}(M,R,T)\right)=\ln\left(SA_{DCPP}(M,R,T)\right)+a_1+a_2 \qquad (6\text{-}8)$$

where $\hat{S}a_{760}(M,R,T)$ is the median spectral acceleration from the NGA models for a V_{S30} of 760 m/s, a_1 is the average amplification (in natural log units) from V_{S30}=760 m/s to V_{S30}=1200 m/s, and a_2 is the site-specific amplification (in natural log units) from an average site with V_{S30}=1200 m/s and kappa=0.04 seconds to the DCPP site. The standard deviation is given by eq. 6-7.

For 5 percent damped spectral acceleration averaged over 3-8.5 Hz, the median is adjusted by the scaling from 5Hz to 3-8.5 Hz and given by

$$\ln\left(\hat{S}a_{DCPP}(M,R,3-8.5Hz)\right)=\ln\left(\hat{S}a_{760}(M,R,5Hz)\right)+a_1+a_2-0.04 \qquad (6\text{-}9)$$

The standard deviation is also adjusted by the difference between the variance for 5 Hz and the variance for 3–8.5 Hz and is given by

$$\sigma_{EQTotal}(3-8.5Hz,M)=\sqrt{\sigma^2(T,M)-\left(1-\frac{1}{N}\right)\sigma_{S2S}^2(T,M)-0.058} \qquad (6\text{-}10)$$

6.6.5 Directivity

There are two parts of the directivity effect: scaling of the average horizontal component and systematic differences between the fault normal and fault parallel components (Somerville et al., 1999). Recently, a directivity model for the scaling on the average horizontal component was developed by Spudich and Chiou (2008) based on the residuals from NGA GMPEs. As part of the NGA project, this directivity model was reviewed by the NGA developers to evaluate its applicability to their NGA GMPEs. The Spudich and Chiou (2008) directivity model has a stronger seismological basis than of Somerville et al. (1999) because it includes a radiation pattern term. An issue with this model is that it is not centered on zero for average directivity conditions, implying a change in the median ground motion for average directivity conditions. The NGA developers were unsure of the cause for this shift and how the Spudich and Chiou (2008) directivity models should be applied to the NGA GMPEs.

Watson-Lamprey (2007) evaluated the within-event residuals from the NGA GMPEs following the same approach as used by Somerville et al. (1999). Watson-Lamprey found that the directivity effect was about one-half as strong as in the Somerville et al. (1999) model. This was not consistent with the strong directivity effects given in the Spudich and Chiou (2008) model.

As a result, the NGA developers did not make recommendations with regard to the applicability of the new directivity models to the NGA GMPEs. Rather, a follow-on project to further evaluate the directivity effect was recommended. This follow-on project began in 2010 and should be completed in 2012. As part of this follow-on project, Abrahamson and Watson-Lamprey developed an update of the Abrahamson (2000) model based on numerical simulations of ground motions conducted as part of the NGA project. This updated model is described in Appendix K. The key feature of this updated model is the use of nonnormalized lengths of rupture toward the site in place of the normalized length parameter, X. The saturation of the directivity is on the nonnormalized lengths. A main change using this revised parameterization is that relative to the NGA model, the directivity effects are strongest for backward directivity (rupture away from the site). That is, the main effect of the new directivity model is that this is a significant reduction of the long period ground motion for sites locate close to the epicenter (backward directivity) but only a small increase for sites in the forward directivity direction.

In ground-motion models, the primary effect of directivity is to increase the variability of the long period ground motion at short distances. The 84th percentile ground motion includes much of the effect of directivity through the standard deviation of the ground motion because the current larger ground-motion data sets better sample the range of directivity conditions in the data. That is, forward directivity leads to an above average ground motion at long periods, and the use of the 84th percentile is addressing this above-average ground motion case.

Given that the directivity models are under review and revision and will only affect the low frequencies that are not critical for nuclear power plants, directivity effects are not included in this analysis. They will be considered in the next full update of the PSHA as part of the LTSP Update.

6.6.6 Effect of New Ground Motion Models

The NGA ground motion models lead to significant changes in the ground motion scaling as compared to GMPEs developed prior to the year 2000. In general, for sites located close to large strike-slip earthquakes, there is a reduction of the median ground motion, but an increase in the standard deviation. For example, Figure 6-15 shows the 84^{th} percentile spectra for the Hosgri fault source from the 1991 LTSP/SSER34 (PG&E, 1988; NRC, 1991) and the 1977 HE design spectrum. The 1991 LTSP/SSER34 spectrum and the 1977 HE design spectrum are similar, but there is a large difference between these two spectra and the Hosgri fault source spectrum computed using the NGA models: using the NGA models, the 84^{th} percentile spectrum is reduced, indicating that previous ground motion models, based on sparse near-fault ground motions, had overestimated the ground motion at short distances.

For reverse faults, the effects are different. Figure 6-16 shows the 84^{th} percentile spectra for the Los Osos fault source based on the 1988 LTSP (PG&E, 1988) ground motion model. The spectrum based on the NGA models is shown with and without hanging wall effects. Excluding hanging wall effects, there is a reduction for the NGA models as compared to the 1988 LTSP model, similar the reduction for strike-slip earthquakes, but a key feature of the NGA models is an increase in the high frequency ground motion for sites located at short distances on the hanging wall side of the rupture. When the hanging wall effects are included, the spectrum is increased to a level that is similar to the spectrum based on the 1988 LTSP ground motion

model. The DCPP is on the hanging wall side of both the Los Osos and San Luis Bay fault sources so the hanging wall effect applies to both fault sources.

These changes in the ground motion affect the relative contribution of strike-slip and reverse faults to the seismic hazard at DCPP. Given the reduction in the near-fault ground motions from strike-slip earthquakes and only small changes in the near-fault ground motions for sites on the hanging wall of reverse earthquakes, the two nearby reverse fault sources (Los Osos and San Luis Bay) will have a larger contribution to the hazard at DCPP relative to the strike-slip Hosgri fault source as compared to the 1988 LTSP (PG&E, 1988).

6.7 Deterministic Ground Motions

The 84th percentile deterministic ground motions for the average horizontal component are computed for each of the four nearby fault sources: Hosgri, Los Osos, San Luis Bay, and Shoreline.

6.7.1 Earthquake Magnitudes

The selection of earthquake magnitude to use in deterministic evaluations involves judgment. In this report, the range in the mean characteristic earthquake magnitude resulting from the source characterization logic tree is considered. The magnitude corresponding to the 90th fractile of the mean characteristic magnitude is selected as a reasonably conservative value for use in the deterministic analysis.

The cumulative distributions of the epistemic uncertainty for the mean characteristic magnitudes for the four fault sources are shown in Figure 6-17. For the Hosgri fault source, the median magnitude is 6.8 and the 90th fractile is magnitude 7.1. This is consistent with the M7.2 magnitude selected for the determinsitic analysis of the Hosgri earthquake in the 1988 LTSP (PG&E, 1988). For the Los Osos fault the median magnitude is M 6.5 and the 90th fractile corresponds to M 6.8.

For the San Luis Bay and Shoreline fault sources, the evaluation is more complicated because the source characterization logic tree includes a branch in which these two faults are linked. For the Shoreline fault, the distribution shown in Figure 6-17 only includes the rupture scenarios that include rupture of the Central segment (e.g. rupture past the DCPP site) from either the independent or linked models. That is, rupture of just the South or just the North segments of the Shoreline fault is not included in the distribution of mean characteristic magnitudes for the development of the deterministic scenario earthquake for the Shoreline fault source. For the Shoreline fault source (including rupture of the Central segment source), the median magnitude is M 6.2 and the 90th fractile corresponds to M 6.4 to M 6.5, which is rounded up to M 6.5.

For the San Luis Bay fault source, the distribution shown in figure 6-17 is for the non-linked case (East and West segments together). The median magnitude is 6.1 and the 90th fractile corresponds to magnitude of 6.3.

The selected deterministic magnitudes for the four fault sources are listed in Table 6-8. The range of dip angles from the logic trees is also listed in this table for each fault source.

6.7.2 Deterministic Ground Motions

The 84th percentile ground motions are computed using the single-station sigma approach with the median given by eq. 6-8 and the standard deviation given by eq. 6-7. For the median from the NGA relations, $Sa_{760}(M,R<T)$,the weighted geometric mean of the spectra from the five NGA models is used. For the standard deviation from the NGA relations, $\sigma(T,M)$, the weighted average (arithmetic mean) from the NGA models is used.

The sensitivity of the ground motion to the dip is shown in Figures 6-18a-c for the Hosgri, Los Osos, and San Luis Bay fault sources, respectively. For all three cases, the lowest dip leads to the largest ground motions at the DCPP site. The uncertainty in the dip of the Los Osos fault source has the largest effect.

For this study, the lowest dip for each fault source is conservatively selected to produce the largest deterministic ground motions at the DCPP site. The geometric mean of the 84th percentile spectra for each of the four fault sources are shown on Figure 6-19. The spectral have a peak at 2.5 Hz that reflects the site-specific amplification shown in Figure 6-14. These 84th percentile spectra are compared to the 1991 LTSP/SSER34 spectrum in Figure 6-19. The 84th percentile spectra based on updated ground motion models and updated source characterizations fall below the 1991 LTSP/SSER34 spectrum.

For comparison, Figure 6-19 also shows the deterministic ground motions computed using the traditional ergodic approach. Accounting for the site-specific amplification observed at DCPP shifts the spectrum to the lower spectral frequencies as compared to the ergodic approach.

6.8 Probabilistic Seismic Hazard Analysis

The probabilistic seismic hazard analysis follows the standard approach first developed by Cornell (1968). This approach has been expanded to more fully treat both the randomness (i.e., aleatory variability) and the scientific uncertainty (i.e., epistemic uncertainty).

6.8.1 Additional Sources

For completeness, additional regional faults are included in the PSHA. The parameters used for these additional faults are listed in Table 6-9. As these faults have a small impact on the hazard, the fault source models are not described in detail.

6.8.2 Hazard Results

The hazard is computed using the program HAZ43 (GEO.DCPP.10.04). The minimum magnitude considered in the hazard calculation is M5.0. This is a commonly used value based on the assumption that earthquakes less than M5.0 will not damage engineered structures.

Figures 6-20a–c show the hazard curves for PGA, 5 Hz, and 1.0 Hz spectral acceleration. The individual contributions to the total hazard from the fault sources are shown on the figures. These plots show that the main contribution to the total hazard is from the Hosgri fault for all hazard levels. The Los Osos, San Luis Bay, and Shoreline faults are similar in terms of their contribution to the hazard. The Uniform Hazard Spectra for hazard levels of 1E-3, 1E-4, and 1E-5 are shown on Figure 6-21.

The deaggregations for the 1E-4 hazard level are shown on Figure 6-22a-c for the PGA, 5 Hz, and 1 Hz spectral acceleration. The deaggregations indicate that the earthquakes with magnitudes between 6.5 and 7.0 at short distances (i.e., 3–5 km) control the hazard at all three spectral periods.

The fragility used in the PRA for DCPP is based on the spectral acceleration averaged over the frequency band of 3–8.5 Hz. The hazard curve for this ground motion parameter is shown on Figure 6-23. To show the impact of the Shoreline fault source, the hazard is shown with and without the Shoreline fault source. The addition of the Shoreline fault source increases the hazard by 20–35 percent for hazard levels of 1E-4 to 1E-5. The epistemic uncertainty in the hazard is shown on Figure 6-24. The epistemic uncertainty in the hazard leads to about a factor of 4 difference between the 10th and 90th fractile. Compared to most sites, this is a tight range, indicating that the hazard at DCPP is relatively well constrained due to the dominance of the Hosgri fault.

Figure 6-25 compares the mean 3-8.5 Hz hazard for the 1988 LTSP (PG&E, 1988) with the mean hazard from this study. The updated hazard curve is lower than the 1988 LTSP hazard curve for spectral acceleration less than about 3g but is higher than the 1988 LTSP hazard curve for spectral accelerations greater than 3g. This figure also compares the mean hazard as computed using the traditional approach with the ergodic standard deviation and ignoring the site-specific amplification with the updated hazard. The traditional approach leads to higher hazard because it does not account for the lower standard deviation and the negative site-specific amplification term.

The epistemic uncertainty of the 3-8.5 Hz hazard from the 1988 LTSP study is compared the epistemic uncertainty from the current study in Figure 6-26. The updated mean hazard curve falls within the 10–90th fractiles from the 1988 LTSP except at very large ground motions (> 3g).

6.9 Seismic Hazard Conclusions

For the deterministic analysis, the new estimates of the 84th percentile ground motion fall below the 1991 LTSP/SSER34 (NRC 1991) deterministic spectrum, indicating that the deterministic seismic margins for the new estimates of the ground motion are at least as large as found during the LTSP (PG&E, 1988, 1991).

For the probabilistic analysis, the hazard for 3–8.5 Hz spectral acceleration is lower than the 1988 LTSP hazard for spectral acceleration less than 3.0 g and is greater than the 1988 LTSP for spectral accelerations greater than 3.0 g. This change in the hazard curve is primarily due to the change in the ground-motion models. The NGA models result in lower median ground motions for sites close to large earthquakes, but with an increased standard deviation. The flattening of the new hazard compared to the 1988 LTSP hazard curves is due to the larger standard deviation.

Because the updated hazard curve is not enveloped by the 1988 LTSP hazard curve, the seismic core damage frequency (CDF) has been reevaluated. The seismic CDF estimated as part of the 1988 LTSP (PG&E, 1988) was 3.8E-5. Using the revised source characterization and ground motion models and with the 1988 LTSP fragility curves, the seismic CDF decreases to about

2.1E-5. The reduction is mainly due to the use the NGA ground motion models with the single-station sigma approach incorporating the site-specific amplification.

Table 6-1a. Coordinates of Fault Sources

Flt	Pt_name	Long	Lat
LosOsos	O1	-120.4590	35.1270
LosOsos	O2	-120.5230	35.1670
LosOsos	O3	-120.6720	35.2220
LosOsos	O4	-120.7090	35.2720
LosOsos	O5	-120.7910	35.3050
LosOsos	O6	-120.9000	35.2990
LosOsos	O7	-120.9950	35.3620
Hosgri	H1	-120.6403	34.6702
Hosgri	H2	-120.8162	35.0443
Hosgri	H3	-121.0177	35.3860
Hosgri	H4	-121.0584	35.4403
Hosgri	H5	-121.0958	35.4961
Hosgri	H6	-121.1381	35.5528
Shoreline	S1	-120.7420	35.1318
Shoreline	S2	-120.7990	35.1769
Shoreline	S3	-120.8740	35.2130
Shoreline	S5	-120.9060	35.2350
Shoreline	S4	-120.9370	35.2563
N40W	S6	-120.9263	35.2642
N40W	S7	-120.9079	35.2418
SLB_East	L6	-120.7142	35.1732
SLB_East	L5	-120.7390	35.1800
SLB_East	L4	-120.7510	35.1790
SLB_East	L3	-120.7690	35.1810
SLB_West	L2	-120.7988	35.1769
SLB_West	L1	-120.8885	35.1953

Table 6-1b. Coordinates of San Luis Bay West Segment Source Models for the Linked Branch

Dip	Crustal Thickness (km)	Top of Fault	Bottom of fault
70	10	S2: -120.799, 35.177, Z=0.0 km	S2: -120.799, 35.177, Z=1.0 km
		L1: -120.889, 35.195, Z=0.0 km	S3: -120.874, 35.213, Z=7.1 km
80	10	S2: -120.799, 35.177, Z=0.0 km	S2: -120.799, 35.177, Z=1.0 km,
		-120.905, 35.191, Z=0.0 km	-120.890, 35.204, Z=10.0 km
		L1: -120.889, 35.195, Z= 0.0 km	S3: -120.874, 35.213, Z=10.0 km
85	10	S2: -120.799, 35.177, Z=0.0 km	S2: -120.799, 35.177, Z=1.0 km
		-120.932, 35.184, Z=0.0 km	-120.913, 35.190, Z=10.0 km
		L1: -120.889, 35.195, Z= 0.0 km	S3: -120.874, 35.213, Z=10.0 km
70	12	S2: -120.799, 35.177, Z=0.0 km	S2: -120.799, 35.177, Z=1.0 km
		L1: -120.889, 35.195, Z= 0.0 km	S3: -120.874, 35.213, Z=7.1 km
80	12	S2:-120.799, 35.177, Z=0.0 km	S2: -120.799, 35.177, Z=1.0 km
		-120.897, 35.193, Z=0.0 km	-120.882, 35.208, Z=12.0 km
		L1: -120.889, 35.195, Z= 0.0 km	S3: -120.874, 35.213, Z=12.0 km
85	12	S2: -120.799, 35.177, Z=0.0 km	S2: -120.799, 35.177, Z=1.0 km
		-120.932, 35.184, Z=0.0 km	-120.913, 35.190, Z=12.0 km
		L1: -120.889, 35.195, Z= 0.0 km	S3: -120.874, 35.213, Z=12.0 km
70	15	S2: -120.799, 35.177, Z=0.0 km	S2: -120.799, 35.177, Z=1.0 km
		L1: -120.889, 35.195, Z= 0.0 km	S3: -120.874, 35.213, Z=7.1 km
80	15	S2: -120.799, 35.177, Z=0.0 km	S2: -120.799, 35.177, Z=1.0 km
		L1: -120.889, 35.195, Z= 0.0 km	S3: -120.874, 35.213, Z=14.7 km
85	15	S2:-120.799, 35.177, Z=0.0 km	S2: -120.799, 35.177, Z=1.0 km
		-120.923, 35.186, Z=0.0 km	-120.905, 35.195, Z=15.0 km
		L1: -120.889, 35.195, Z= 0.0 km	S3: -120.874, 35.213, Z=15.0 km

Table 6-2a. Depth Limits of the San Luis Bay Fault Source

Depth to the Bottom of the Fault Source (km)	San Luis Bay Fault Source Dip	Los Osos Fault Source Dip	Depth of Intersection of San Luis Bay and Los Osos Fault Sources (km)
10	50	45	5.1
10	70	45	6.8
10	80	45	7.9
10	50	60	6.6
10	70	60	9.9
10	80	60	10
10	50	75	8.4
10	70	75	10
10	80	75	10
12	50	45	5.1
12	70	45	6.8
12	80	45	7.9
12	50	60	6.6
12	70	60	9.9
12	80	60	12
12	50	75	8.4
12	70	75	12
12	80	75	12
15	50	45	5.1
15	70	45	6.8
15	80	45	7.9
15	50	60	6.6
15	70	60	9.9
15	80	60	12.3
15	50	75	8.4
15	70	75	14.7
15	80	75	15

Table 6-2b. Depth Limits of the San Luis Bay East Segment Source

Depth to the Bottom of the Fault Source (km)	San Luis Bay Fault Source Dip	Los Osos Fault Source Dip	Depth of Intersection of SLB and Los Osos Fault Sources (km)
10	83	45	8.2
10	83	60	10
10	83	75	10
12	83	45	8.2
12	83	60	12
12	83	75	12
15	83	45	8.2
15	83	60	13.3
15	83	75	15

Table 6-3. Magnitude-Area Scaling Relations

	Sense of Slip	Model	Standard error of constant coeff
Hanks and Bakun (2008)	SS	M = 3.98 + 1.0 log(A) for A<537 km^2 M = 3.07 + 4/3 log(A) for A>537 km^2	Not given
Wells and Coppersmith (1994)	SS	M = 3.98 + 1.02 log(A)	0.07
	RV	M = 4.33 + 0.90 log(A)	0.12
	ALL	M = 4.07 + 0.98 log(A)	0.06
Wells and Coppersmith (1994)	ALL	log(Area) = 0.91M – 3.49 (σ=0.24)	
		log (Width) = 0.32 M – 1.01 σ=0.15)	

Table 6-4. Computed V_{S30} Values (for 10 m Embedment) for the Power Block and the ISFSI Borehole Sites

	V_{S30} (m/s) for 10 m Embedment (Applicable to the Power Block)
Power Block	1210
ISFSI 98BA-1&4	1225
ISFSI 98BA-3	1214

Table 6-5. Smoothed Coefficients for the Amplification from V_{S30}=760 m/s to V_{S30}=1200 m/s

Period (sec)	Freq (Hz)	a_1 for V_{S30}=1200 m/s	a_1 for V_{S30}=1100 m/s
0.01	100.00	-0.35	-0.28
0.02	50.00	-0.35	-0.29
0.03	33.33	-0.35	-0.28
0.05	20.00	-0.26	-0.21
0.075	13.33	-0.26	-0.19
0.10	10.00	-0.27	-0.26
0.15	6.67	-0.29	-0.33
0.20	5.00	-0.31	-0.21
0.25	4.00	-0.34	-0.28
0.30	3.33	-0.37	-0.36
0.40	2.50	-0.4	-0.37
0.50	2.00	-0.42	-0.44
0.75	1.33	-0.42	-0.34
1.0	1.00	-0.36	-0.22
1.5	0.67	-0.27	-0.17
2.0	0.50	-0.21	-0.28
3.0	0.33	-0.130	-0.12
4.0	0.25	-0.080	-0.07
5.0	0.20	-0.045	-0.04
10.0	0.10	0	0
	3-8.5 Hz	-0.33	

Table 6-6. Event terms for the 2004 Parkfield and 2003 San Simeon Earthquakes.

			Parkfield Eqk, R40-170 Km, Event Terms			
T (sec)	Freq (Hz)	Nb Rec.	AS08	BA08	CB08	CY08
0.01	100	18	-0.2971	-0.7524	-0.7688	-0.1765
0.02	50	18	-0.2898	-0.7530	-0.7675	-0.1702
0.03	33.33	18	-0.2941	-0.7690	-0.7907	-0.1849
0.05	20	18	-0.2776	-0.7911	-0.8289	-0.2049
0.075	13.33	18	-0.2766	-0.8499	-0.8573	-0.2390
0.1	10	18	-0.2232	-0.7846	-0.7911	-0.1942
0.15	6.67	18	-0.2741	-0.7841	-0.7964	-0.2434
0.2	5	18	-0.3236	-0.8568	-0.7760	-0.2476
0.3	3.33	18	-0.3315	-0.8572	-0.7160	-0.2539
0.4	2.5	18	-0.2717	-0.7147	-0.5960	-0.2082
0.5	2	18	-0.1896	-0.6215	-0.5083	-0.1361
0.75	1.33	18	-0.0639	-0.4461	-0.3200	-0.0195
1	1	18	-0.0139	-0.3819	-0.2253	0.0092
1.5	0.67	18	0.1138	-0.3449	-0.1050	0.0694
2	0.5	18	0.1144	-0.3242	-0.0415	0.0856

			San Simeon, R0-100 Km, Event Terms			
T (sec)	Freq (Hz)	Nb Rec.	AS08	BA08	CB08	CY08
0.01	100	8	-0.3698	-0.4583	-0.8430	-0.1708
0.02	50	8	-0.3657	-0.4589	-0.8459	-0.1680
0.03	33.33	8	-0.3672	-0.4622	-0.8662	-0.1796
0.05	20	8	-0.3762	-0.5076	-0.9557	-0.2495
0.075	13.33	8	-0.4395	-0.6169	-1.0644	-0.3716
0.1	10	8	-0.5304	-0.6978	-1.1368	-0.4773
0.15	6.67	8	-0.6755	-0.7932	-1.1882	-0.5938
0.2	5	8	-0.6961	-0.8702	-1.1355	-0.5252
0.3	3.33	8	-0.6590	-0.8379	-1.0289	-0.4165
0.4	2.5	8	-0.4285	-0.5533	-0.7384	-0.1767
0.5	2	8	-0.3993	-0.5396	-0.6892	-0.1470
0.75	1.33	8	-0.1099	-0.2415	-0.3086	0.1410
1	1	8	0.0627	-0.0472	-0.0589	0.2835
1.5	0.67	8	0.1122	0.0918	0.0450	0.2448
2	0.5	8	0.1367	0.1403	0.1198	0.3423

Table 6-7. Site-specific site amplification terms and total variance reduction for the single-station sigma approach.

Frequency (Hz)	Smoothed a_2	σ_{S2S} (ln units)	Var Added to NGA Models (ln units)
100	-0.06	0.080	-0.040
50	-0.06	0.079	-0.040
34	-0.06	0.081	-0.041
20	-0.24	0.084	-0.042
13.33	-0.24	0.087	-0.044
10	-0.24	0.089	-0.045
6.67	-0.20	0.090	-0.045
5	-0.18	0.092	-0.046
4	-0.07	0.092	-0.046
3.33	0.05	0.093	-0.047
2.5	0.34	0.094	-0.047
2	0.43	0.096	-0.048
1.33	0.55	0.099	-0.050
1	0.40	0.103	-0.051
0.67	0.40	0.106	-0.053
0.5	0.40	0.109	-0.065
3-8.5	-0.11	0.093	-0.047

Table 6-8. Selected Deterministic Earthquake Scenarios

Fault Source	Magnitude	Dip	Smallest R_{Rup} (km)	Smallest RJB (km)	Rx	Sense of Slip	Hanging Wall or Foot Wall
Hosgri	7.1	80	4.9	2.3	4.9	SS	HW N/A for 90
		85	4.9	3.6	4.9		
		90	4.9	4.9	4.9		
Los Osos	6.8	45	7.6	0.0	9.9	RV/OBL	HW
		60	8.9	2.6	9.9		
		75	9.7	6.5	9.9		
San Luis Bay (not linked)	6.3	50	1.9	0.0	2.5	RV	HW
		70	2.4	0.0	2.5		
		80	2.5	0.0	2.5		
Shoreline	6.5	90	0.6	0.6	0.6	SS	N/A

Table 6-9. Source Parameters for Other Regional Fault Sources

Fault Source	Dip	Depth to Bottom of the Fault Source (km)	Slip-Rate (mm/yr)	Mean Characteristic Magnitude	Sense of Slip
Oceanic	35 (0.3) 45 (0.4) 55 (0.3)	10 (1.0)	0.1 (0.25) 0.3 (0.50) 0.6 (0.25)	6.4 (0.3) 6.8 (0.4) 7.0 (0.3)	RV/OBL (1.0)
West Huasna	90 (1.0)	10 (1.0)	0.5 (0.25) 1.0 (0.50) 2.0 (0.25)	6.6 (0.3) 6.9 (0.4) 7.2 (0.3)	SS (1.0)
Wilmar Ave	45 (1.0)	10 (1.0)	0.1 (0.25) 0.2 (0.50) 0.3 (0.25)	6.4 (0.3) 6.7 (0.4) 7.0 (0.3)	RV (1.0)
Oceano	45 (1.0)	10 (1.0)	0.1 (0.25) 0.2 (0.50) 0.3 (0.25)	6.6 (0.3) 6.9 (0.4) 7.2 (0.3)	RV (1.0)
San Andreas 1857	90 (1.0)	12 (1.0)	31 (0.25) 34 (0.50) 37 (0.25)	7.7 (0.3) 7.8 (0.4) 7.9 (0.3)	SS (1.0)
San Andreas Parkfield	90 (1.0)	12(1.0)	3* (0.25) 4* (0.50) 5* (0.25)	5.9 (0.3) 6.0 (0.4) 6.1 (0.3)	SS (1.0)

* Equivalent slip-rate for mean recurrence intervals of 25, 30, and 40 years

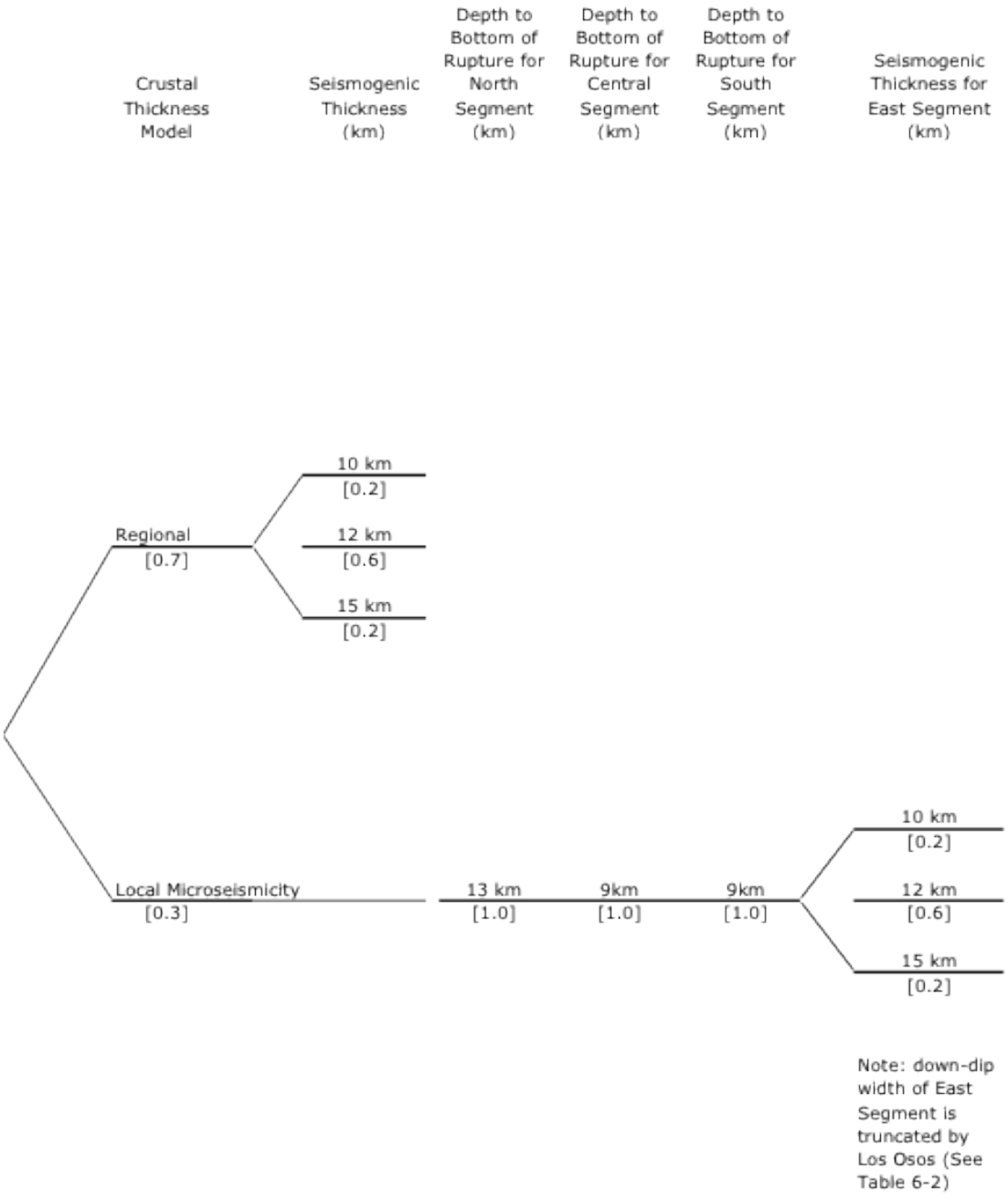

Figure 6-1. Simplified logic tree for the Shoreline fault source

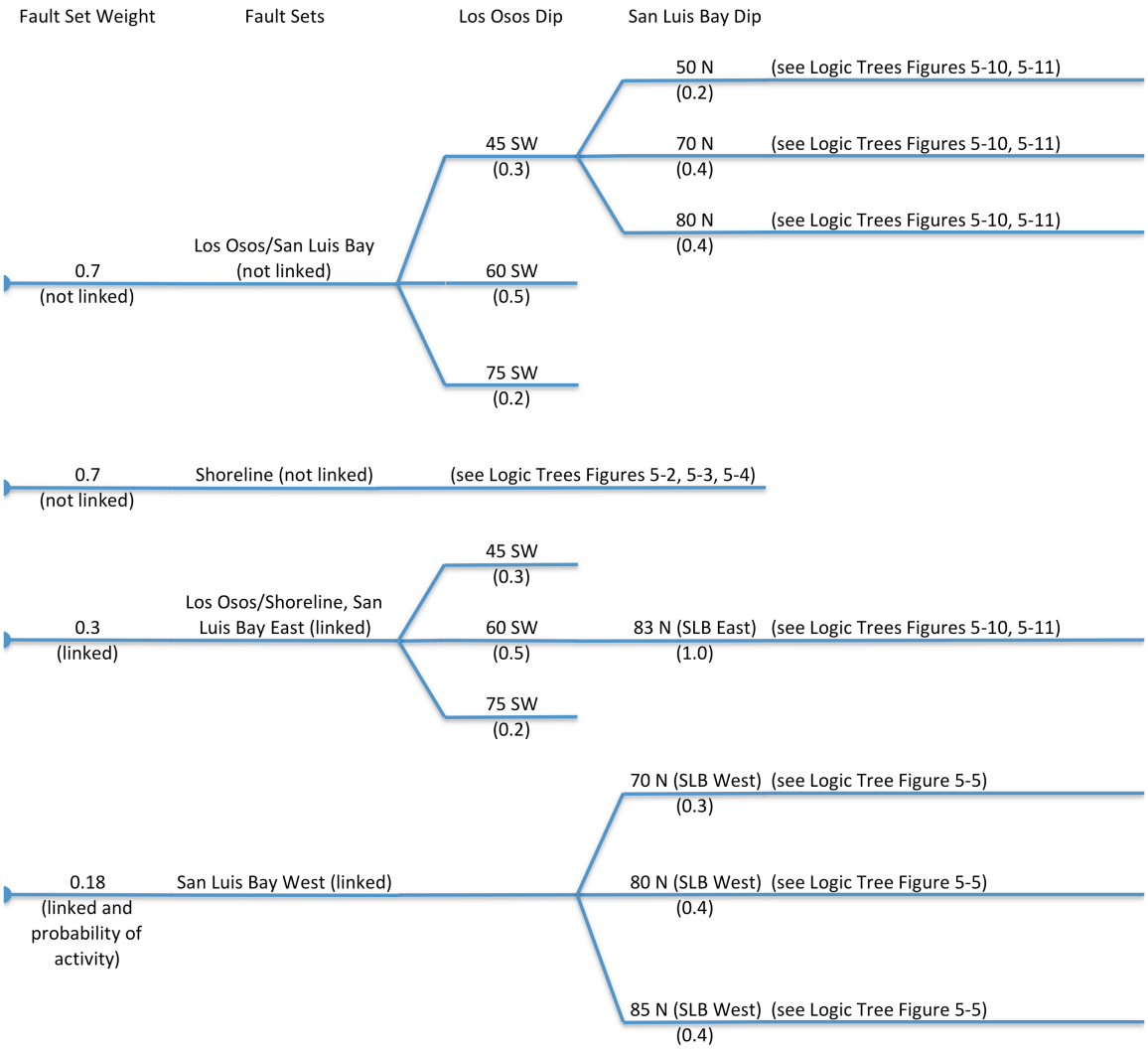

Figure 6-2. Logic tree for ruptures for Shoreline and San Luis Bay fault sources

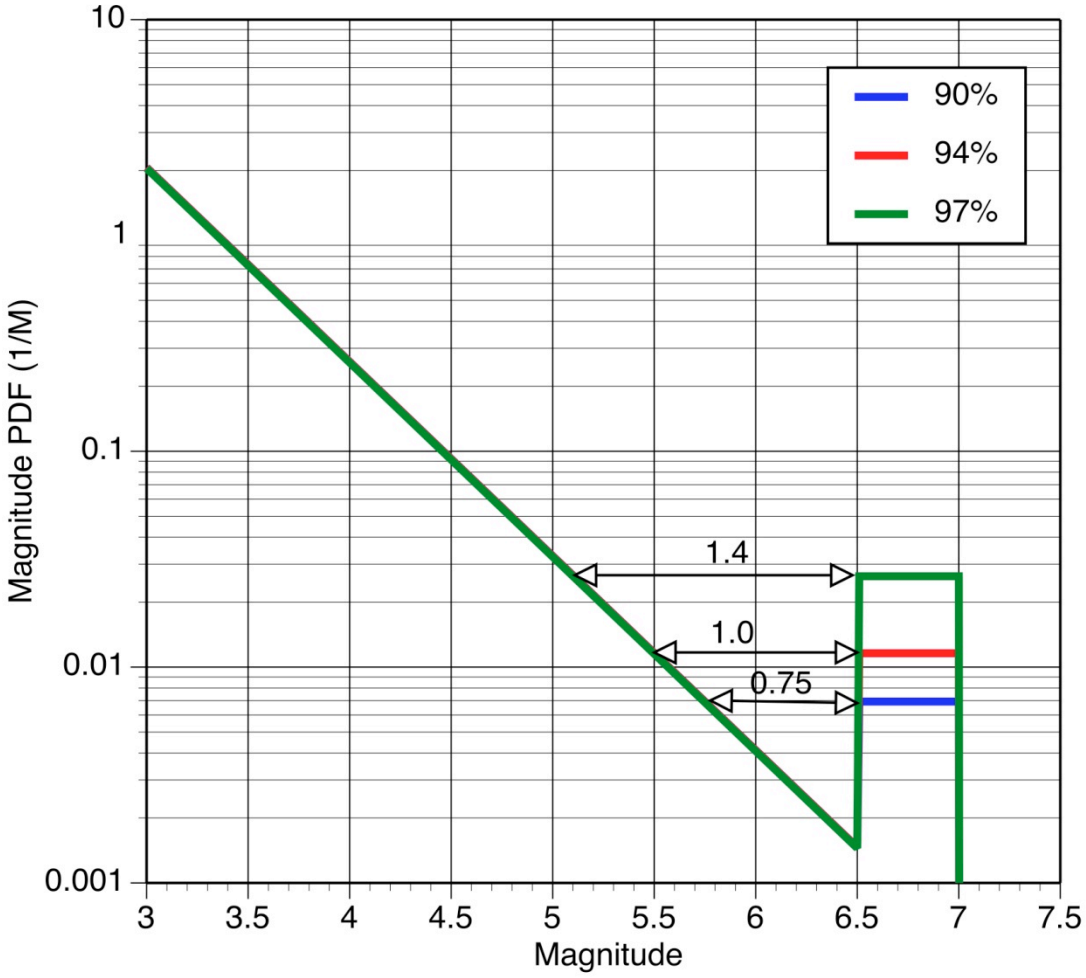

Figure 6-3. Magnitude probability density functions for different percentages of the seismic moment being released in characteristic earthquakes. The Youngs and Coppersmith (1985) model corresponds to the case with 94% of the moment in characteristic earthquakes (red curve).

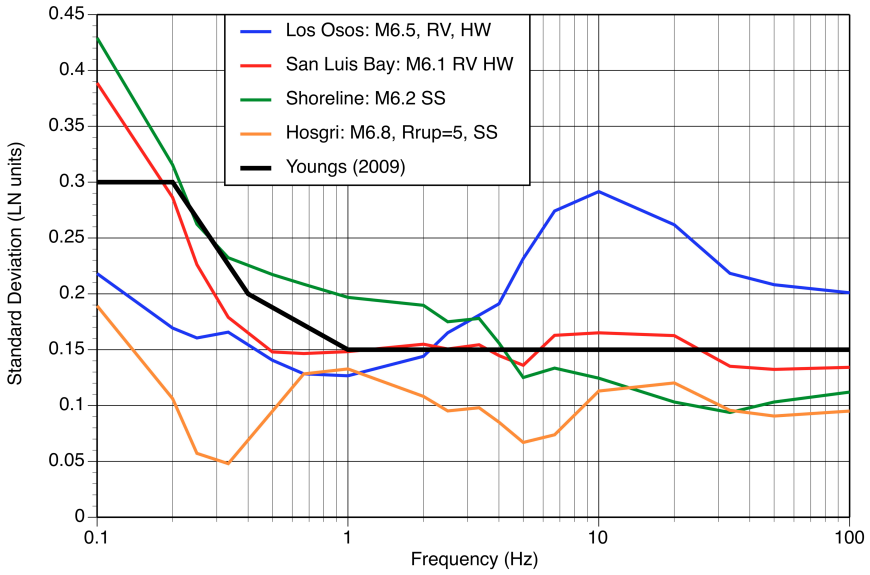

Figure 6-4a. Standard deviation of the median ground motion from the NGA models for representative earthquakes for the four nearby fault sources.

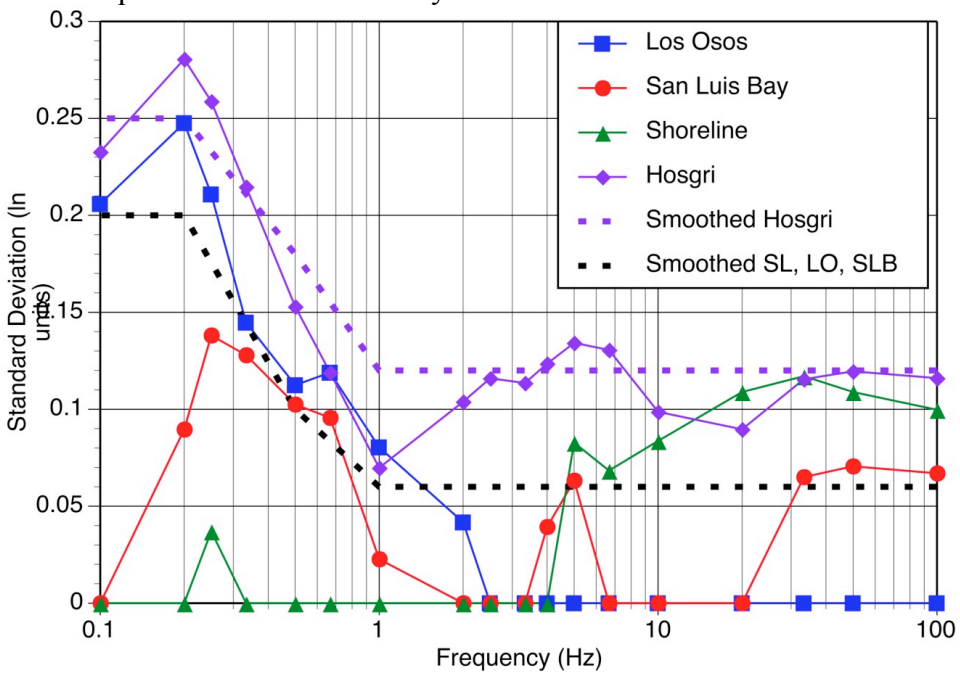

Figure 6-4b. Standard deviation of the addition epistemic uncertainty for the NGA models. The smoothed models for the two groups of fault sources are shown.

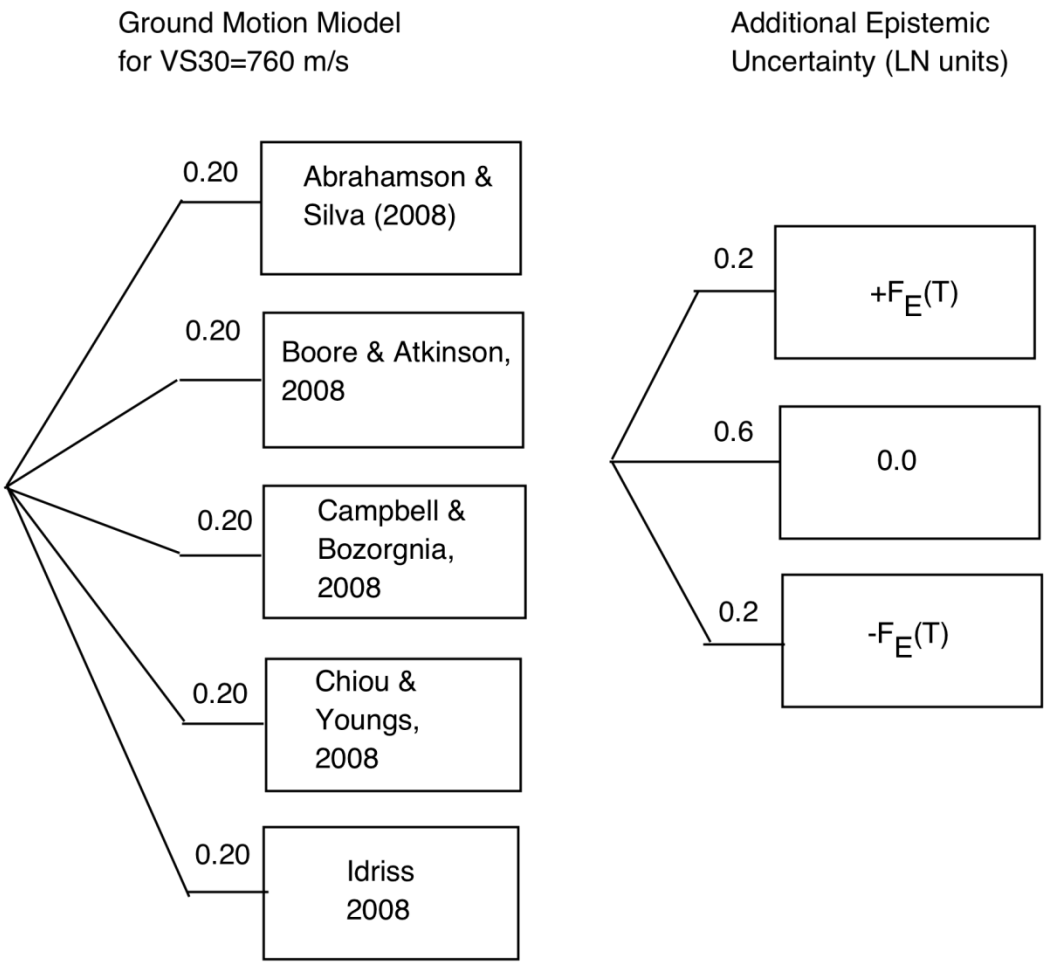

Figure 6-5. Logic tree for ground motion models for crustal earthquakes

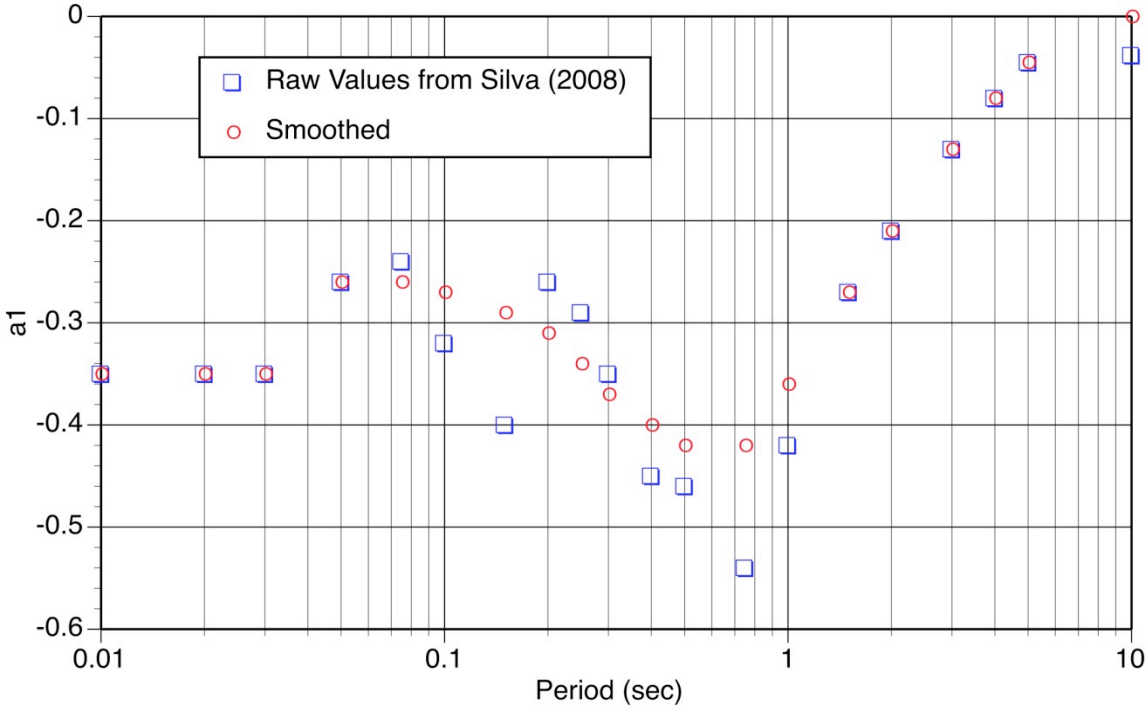

Figure 6-6. Smoothed model of the coefficient for the amplification from V_{S30}=760 m/s to V_{S30}=1200 m/s

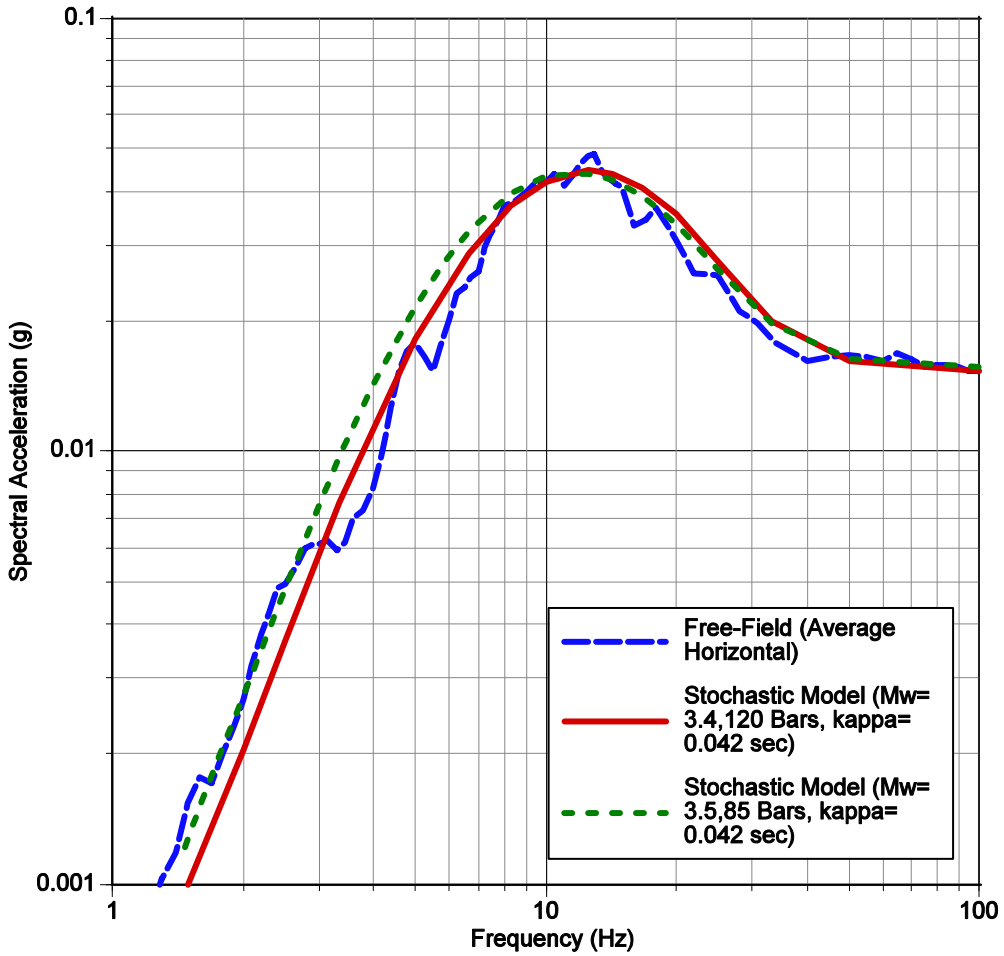

Figure 6-7. Comparison of the average horizontal response spectrum at 5% damping for the free-field recording with the expected California rock site spectrum from a moment magnitude 3.4 earthquake at a distance of 7.8 km with a stress-drop of 120 bars and kappa of 0.042 sec based on the stochastic point source model (red curve). The green curve shows the spectrum if the moment magnitude is 3.5 with a stress-drop of 85 bars. (From Appendix L-1).

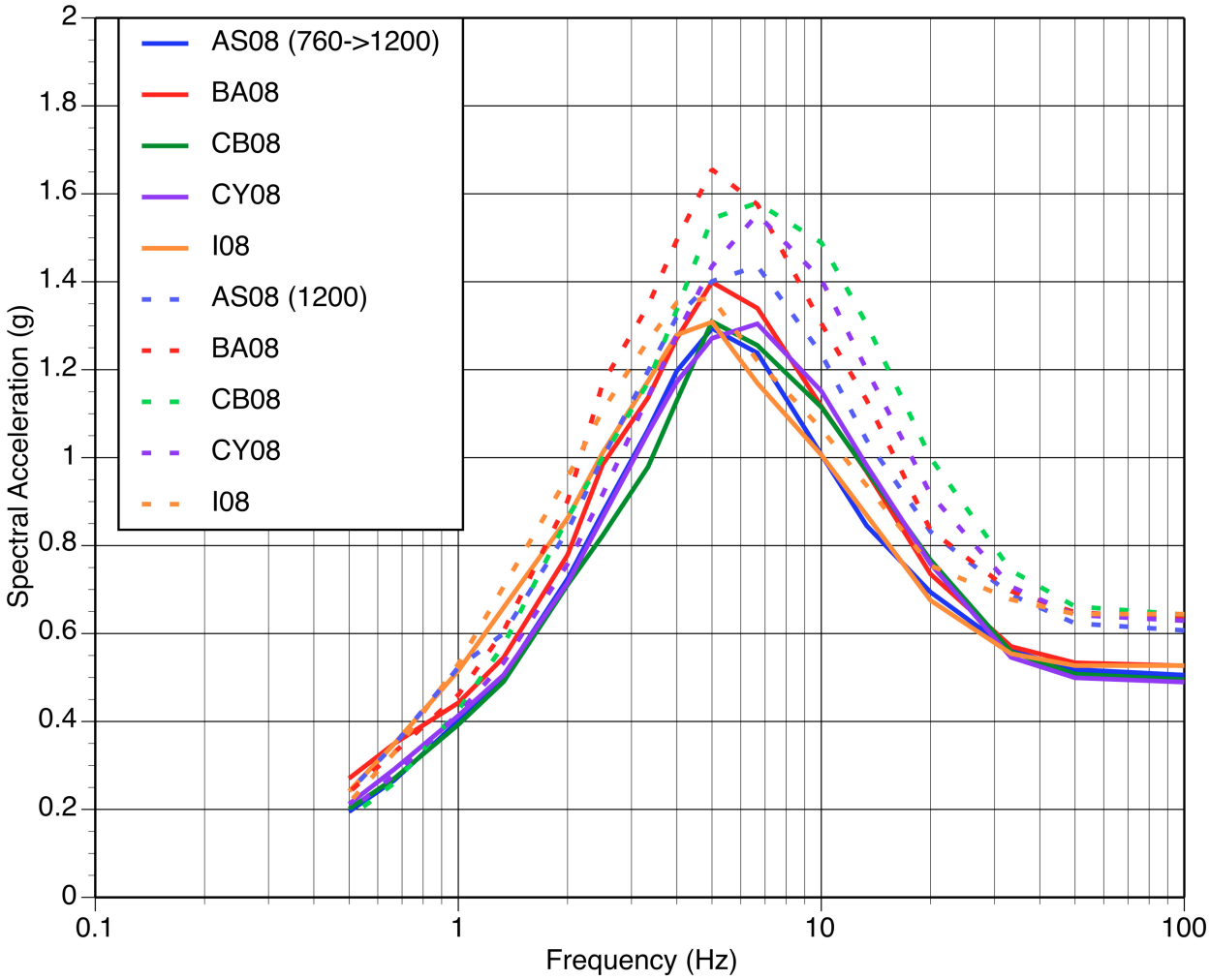

Figure 6-8. Example of effect of the site-specific hard-rock approach (solid lines) versus extrapolating the V_{S30} scaling (dashed lines) for the five NGA models. This example is for a M7.1 SS earthquake at a distance of 4.9 km.

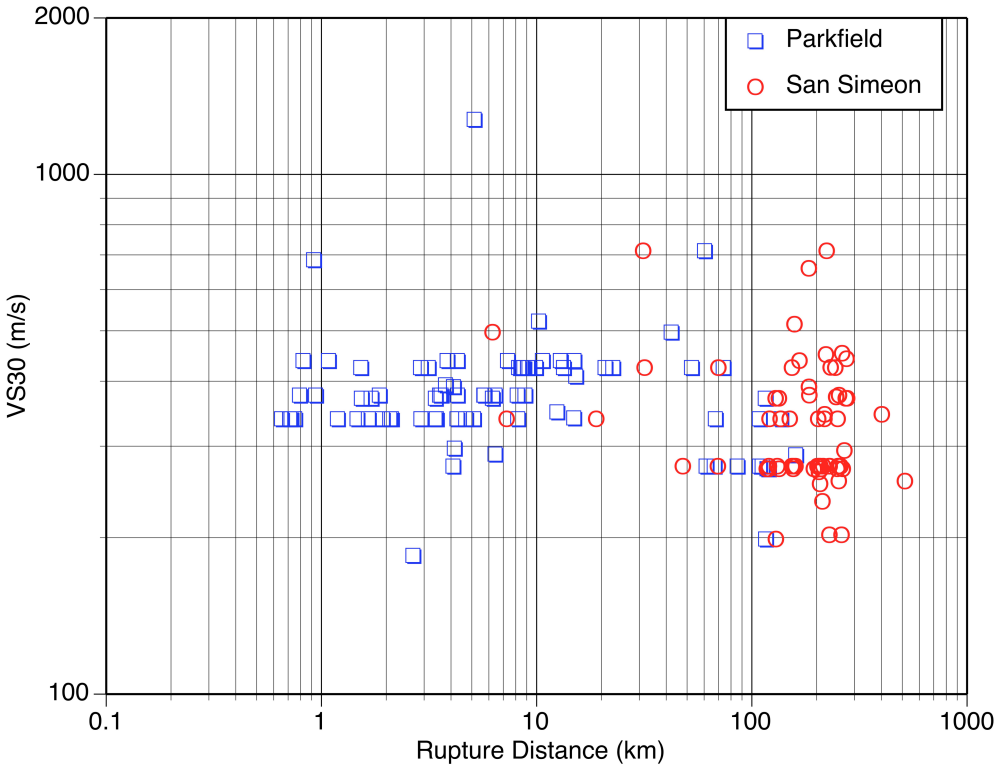

Figure 6-9. Distribution of distances and site conditions for the 2003 San Simeon and 2004 Parkfield earthquakes.

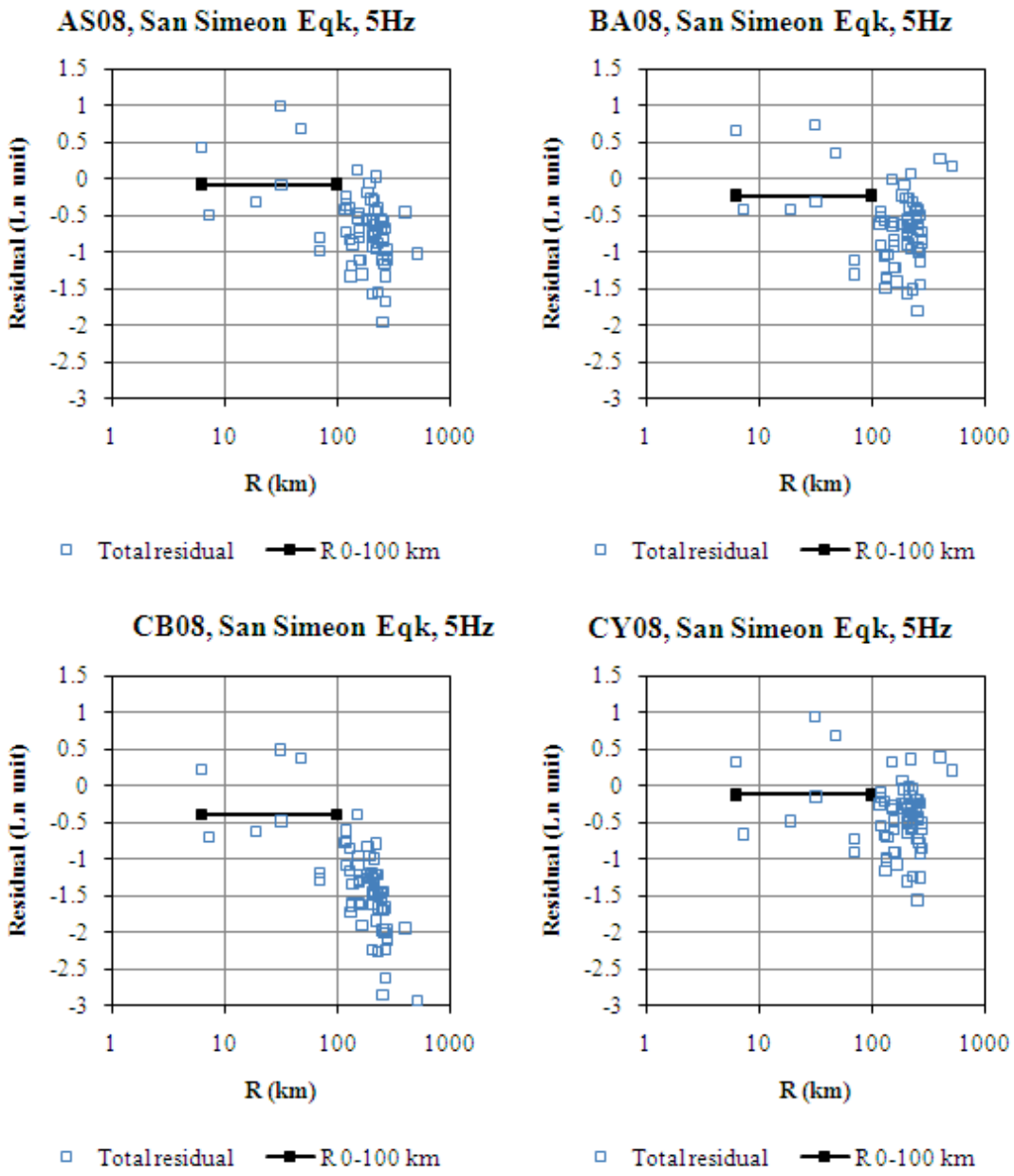

Figure 6-10a. Residuals from the 2003 San Simeon earthquake for 5 Hz spectral acceleration. The rupture distance to DCPP is 35 km. The average residual for stations at distance of 0 to 100 km is shown by the black line.

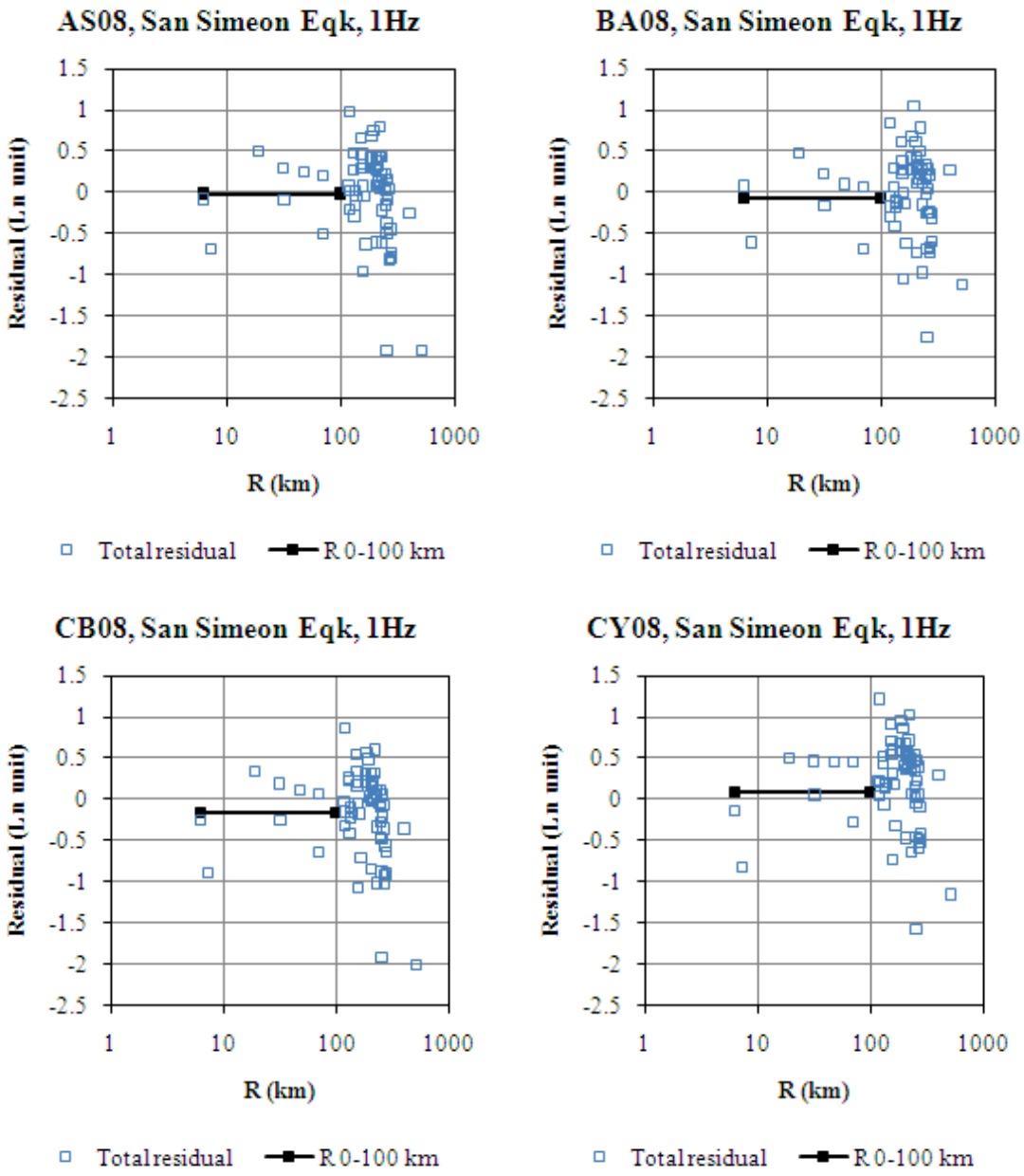

Figure 6-10b. Residuals from the 2003 San Simeon earthquake for 1 Hz spectral acceleration. The rupture distance to DCPP is 35 km. The average residual for stations at distance of 0 to 100 km is shown by the black line.

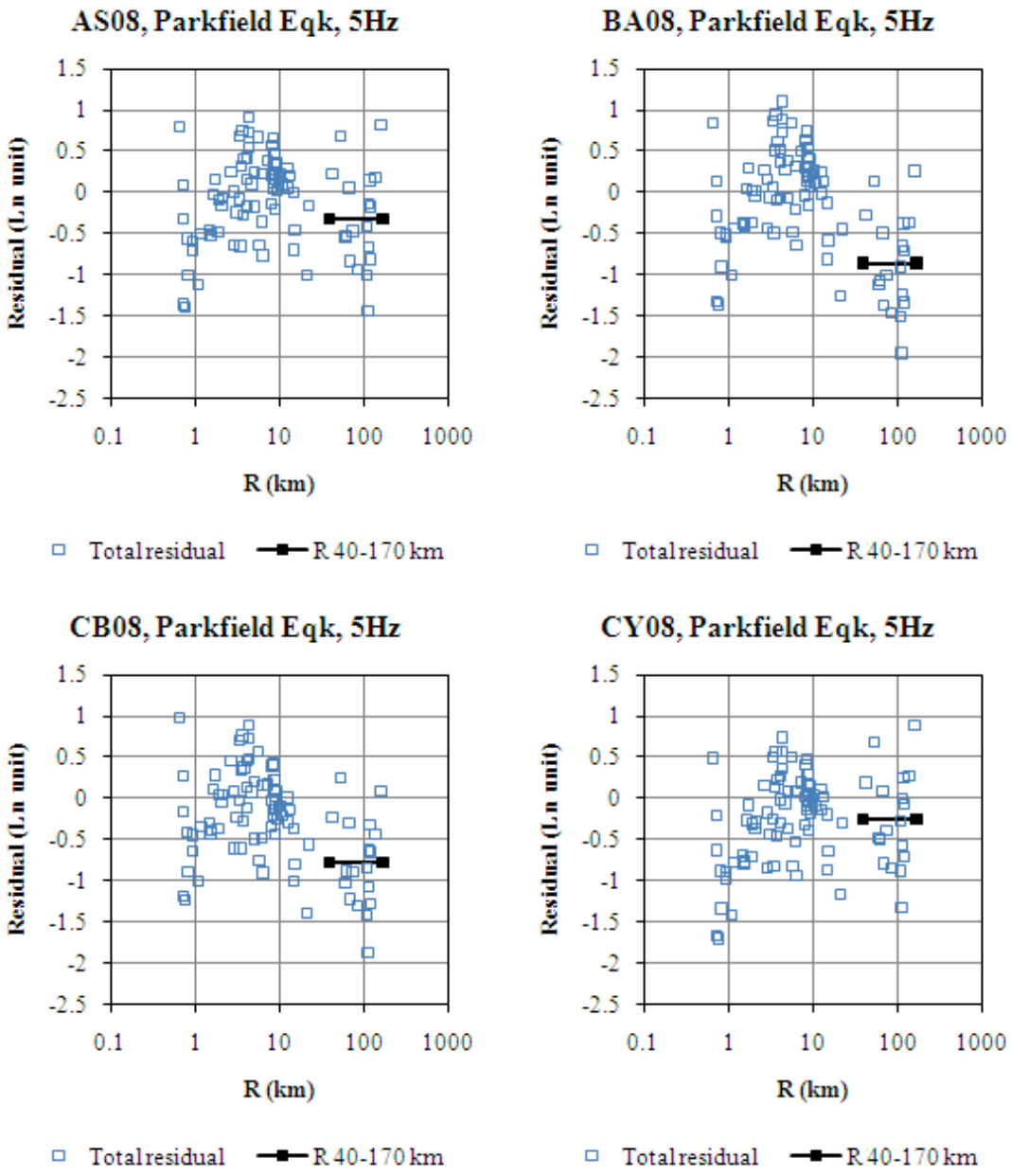

Figure 6-11a. Residuals from the 2004 Parkfield earthquake for 5 Hz spectral acceleration. The rupture distance to DCPP is 85 km. The average residual for stations at distance of 40 to 170 km is shown by the black line.

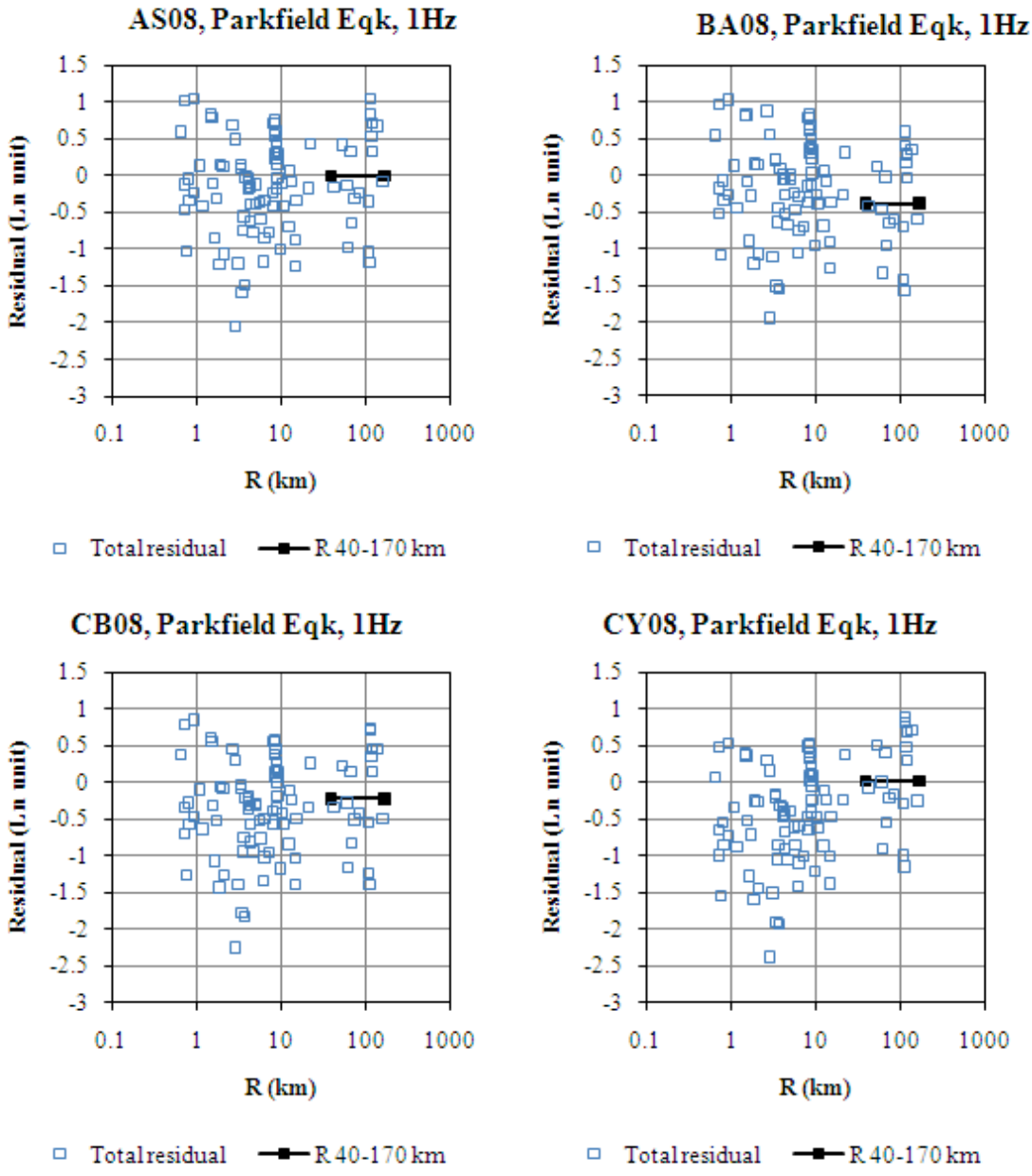

Figure 6-11b. Residuals from the 2004 Parkfield earthquake for 1 Hz spectral acceleration. The rupture distance to DCPP is 85 km. The average residual for stations at distance of 40 to 170 km is shown by the black line.

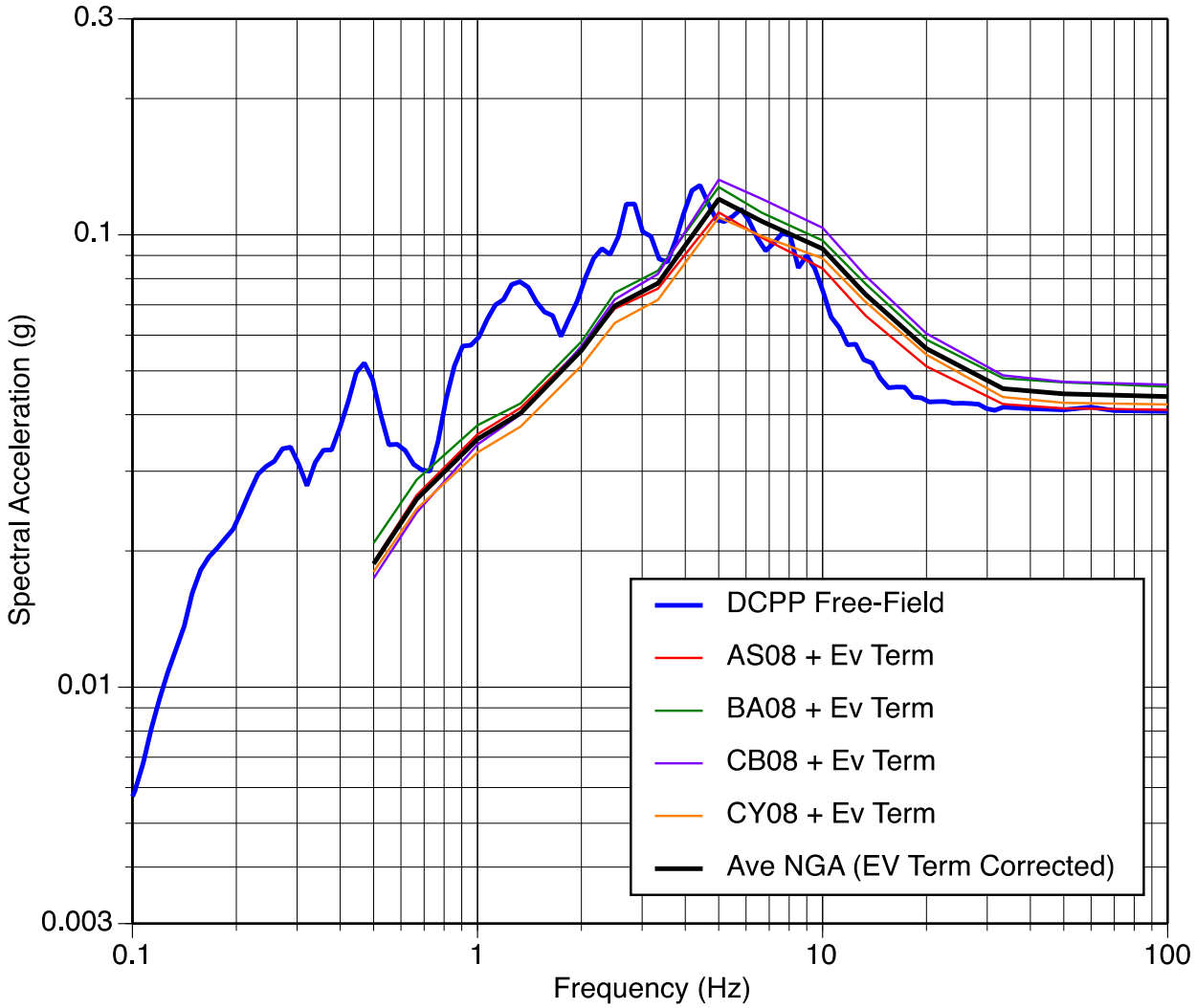

Figure 6-12. Comparison of the event-term adjusted medians from the NGA models with the observed ground motions from the 2003 San Simeon earthquake.

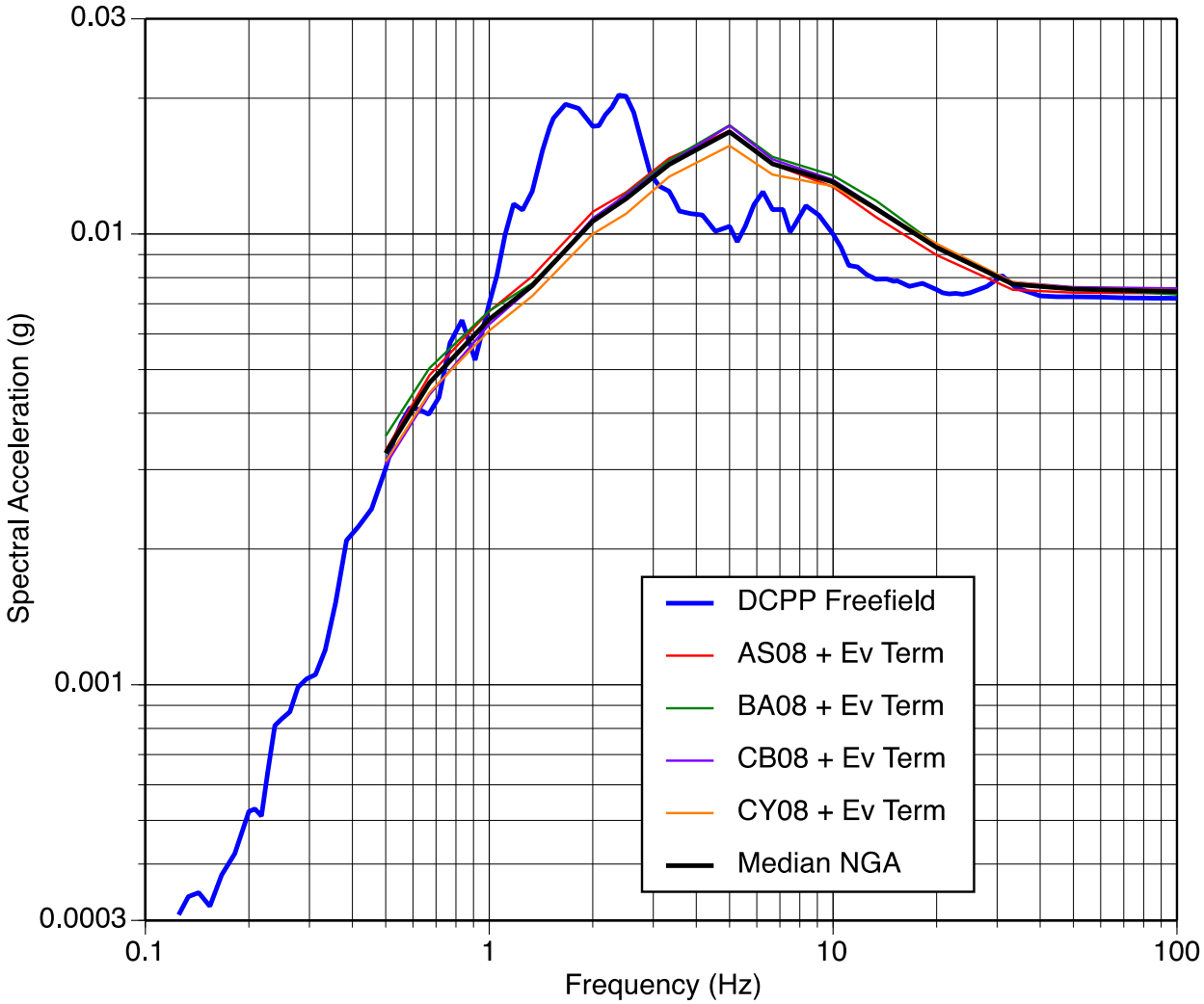

Figure 6-13. Comparison of the event-term adjusted medians from the NGA models with the observed ground motions from the 2004 Parkfield earthquake.

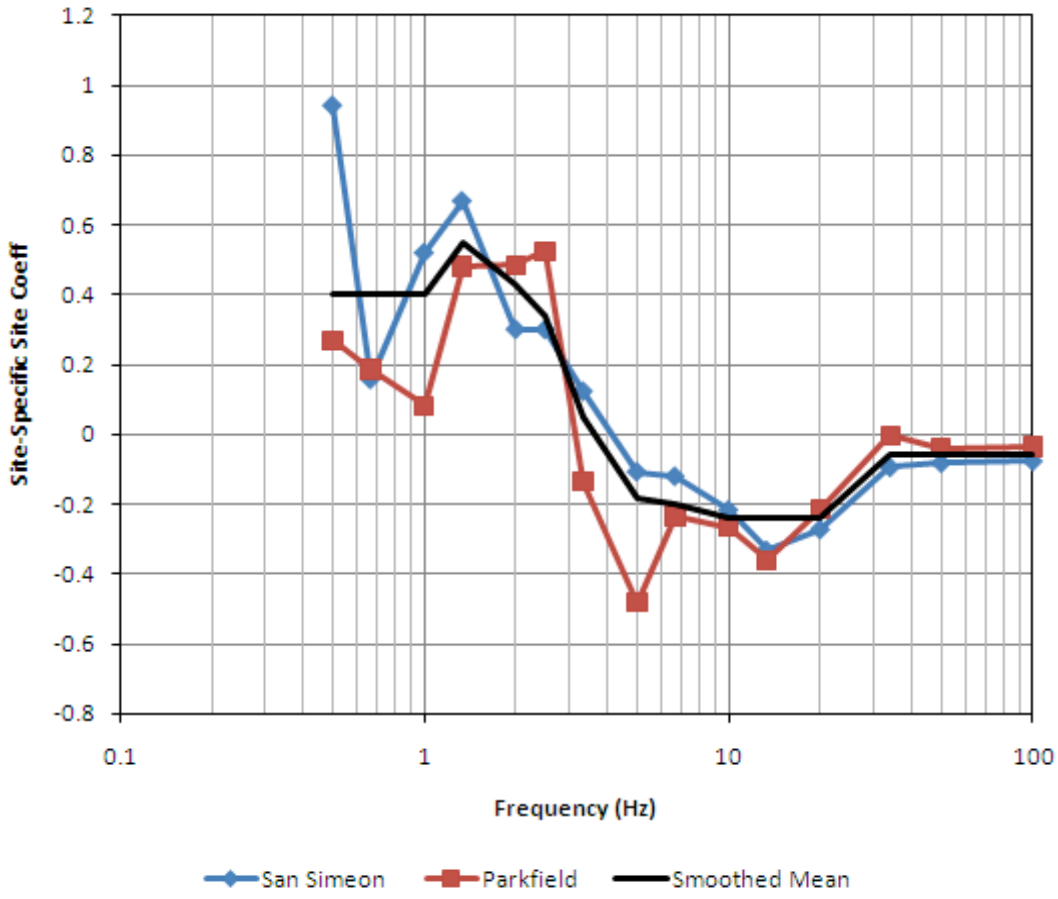

Figure 6-14. Site-specific site amplification terms for DCPP. This shows that the rock site response at DCPP leads to amplified low frequencies (< 0.3 Hz) and reduced high frequencies (5-30 Hz) as compared to average rock sites with V_{S30}=1200 and kappa = 0.04 sec.

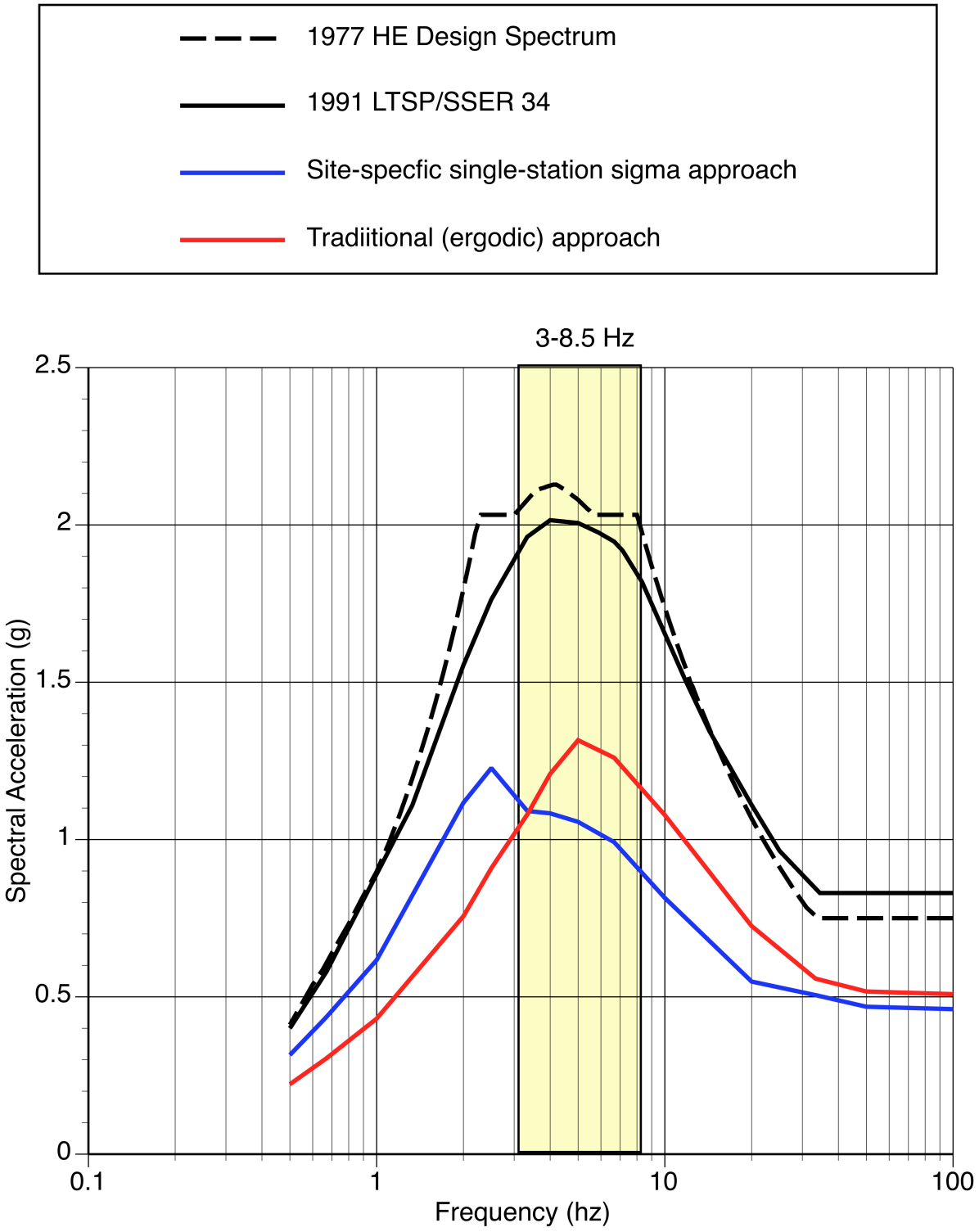

Figure 6-15. Effect of the NGA ground motion models and the site-specific single-station approach for estimating hard-rock motions for nearby strike-slip as compared to the HE design spectrum and the LTSP/SSER spectrum. This example is for a magnitude 7.1 strike-slip earthquake at a distance of 5 km.

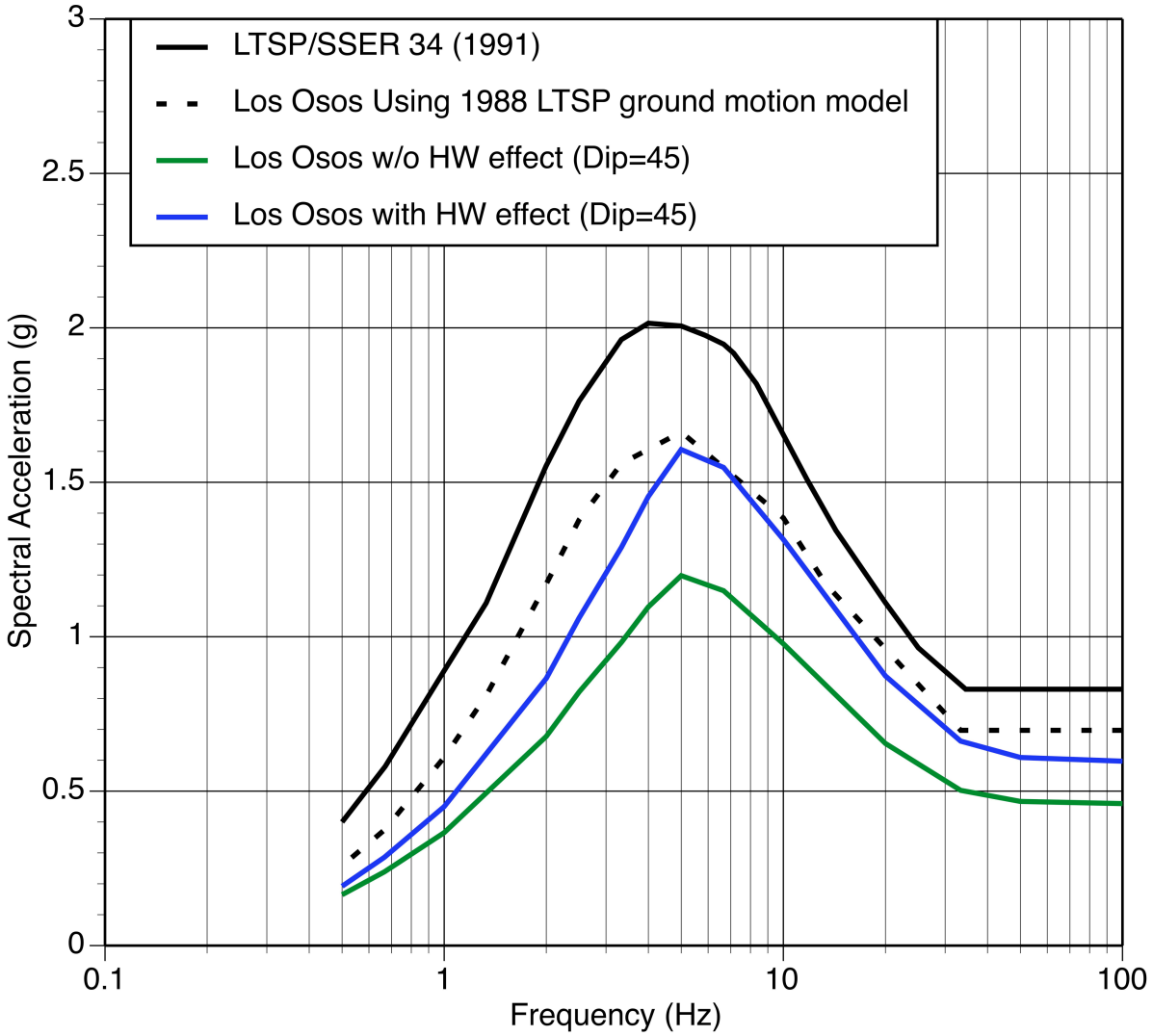

Figure 6-16. Effect of the NGA ground motion models for the Los Osos fault source for the traditional ergodic approach. The hanging wall effect included in the NGA models leads to larger high-frequency ground motions for sites on the hanging wall.

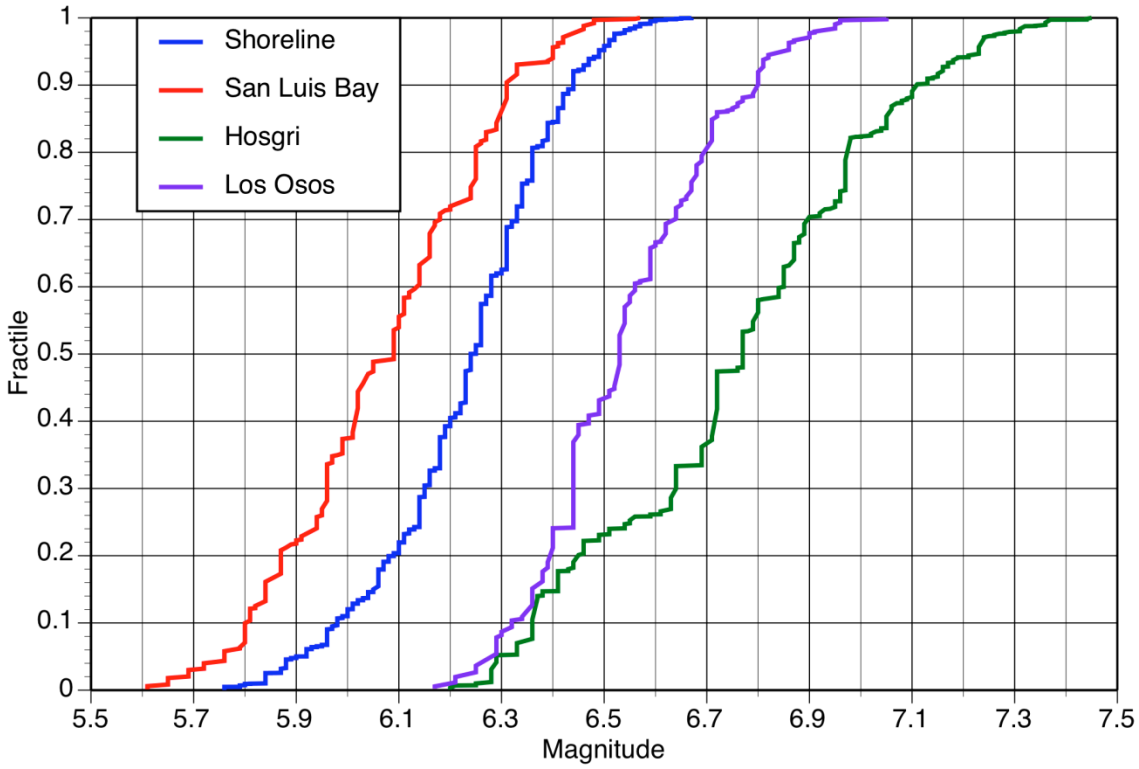

Figure 6-17. Magnitude fractiles from the logic trees for four fault sources

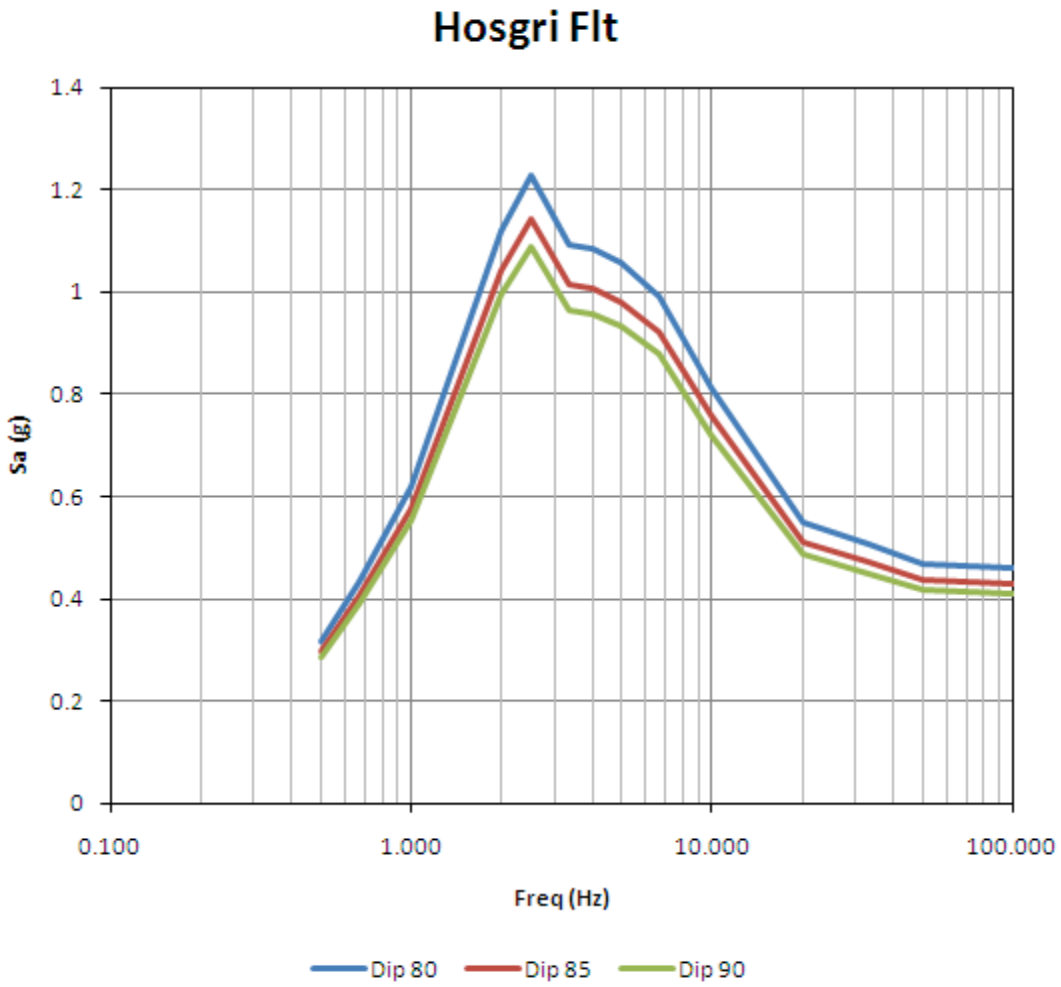

Figure 6-18a. Sensitivity of the deterministic ground motions to the dip of the Hosgri fault source.

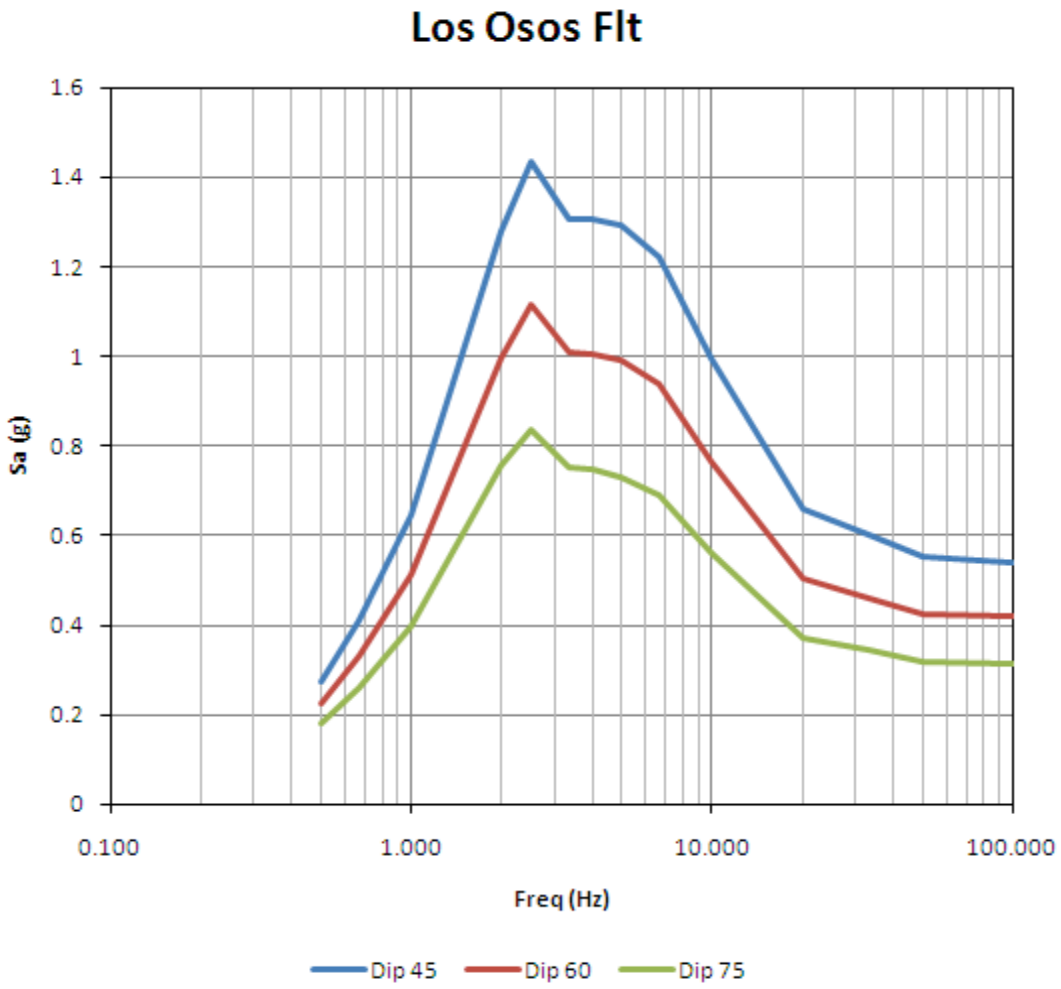

Figure 6-18b. Sensitivity of the deterministic ground motions to the dip of the Los Osos fault source.

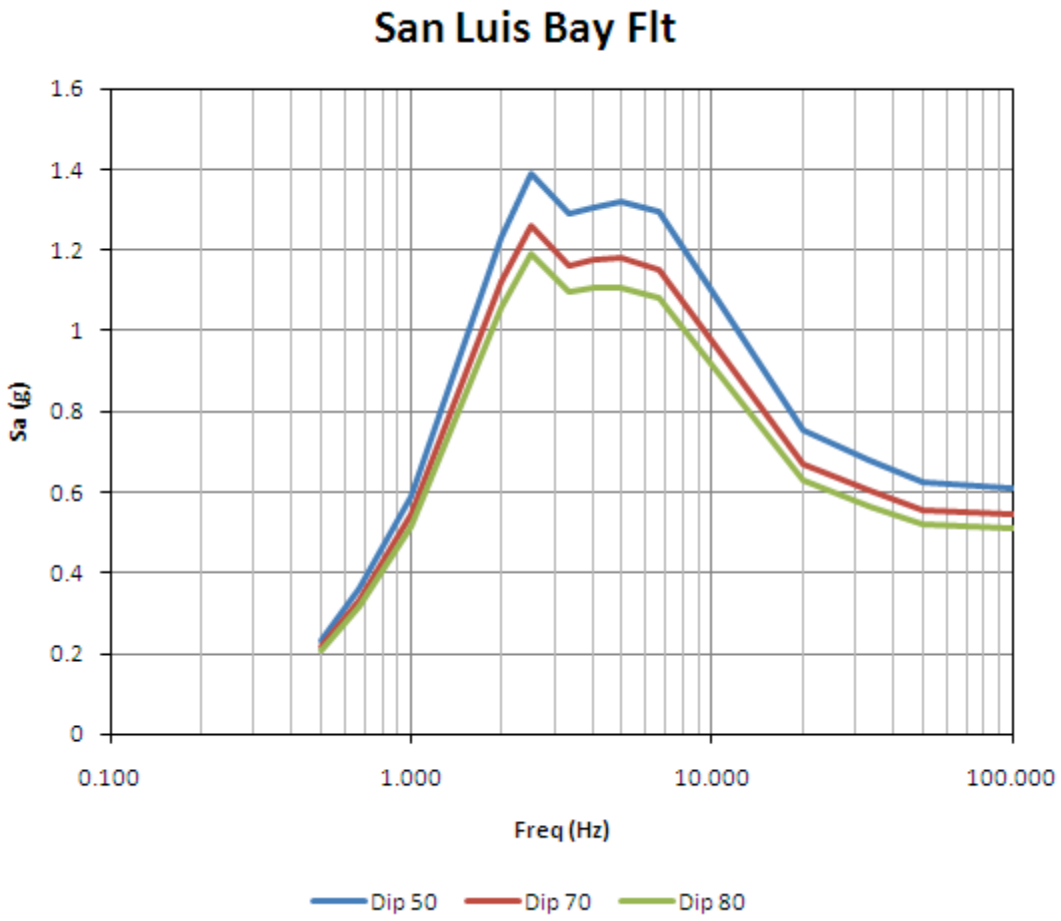

Figure 6-18c. Sensitivity of the deterministic ground motions to the dip of the San Luis Bay fault source.

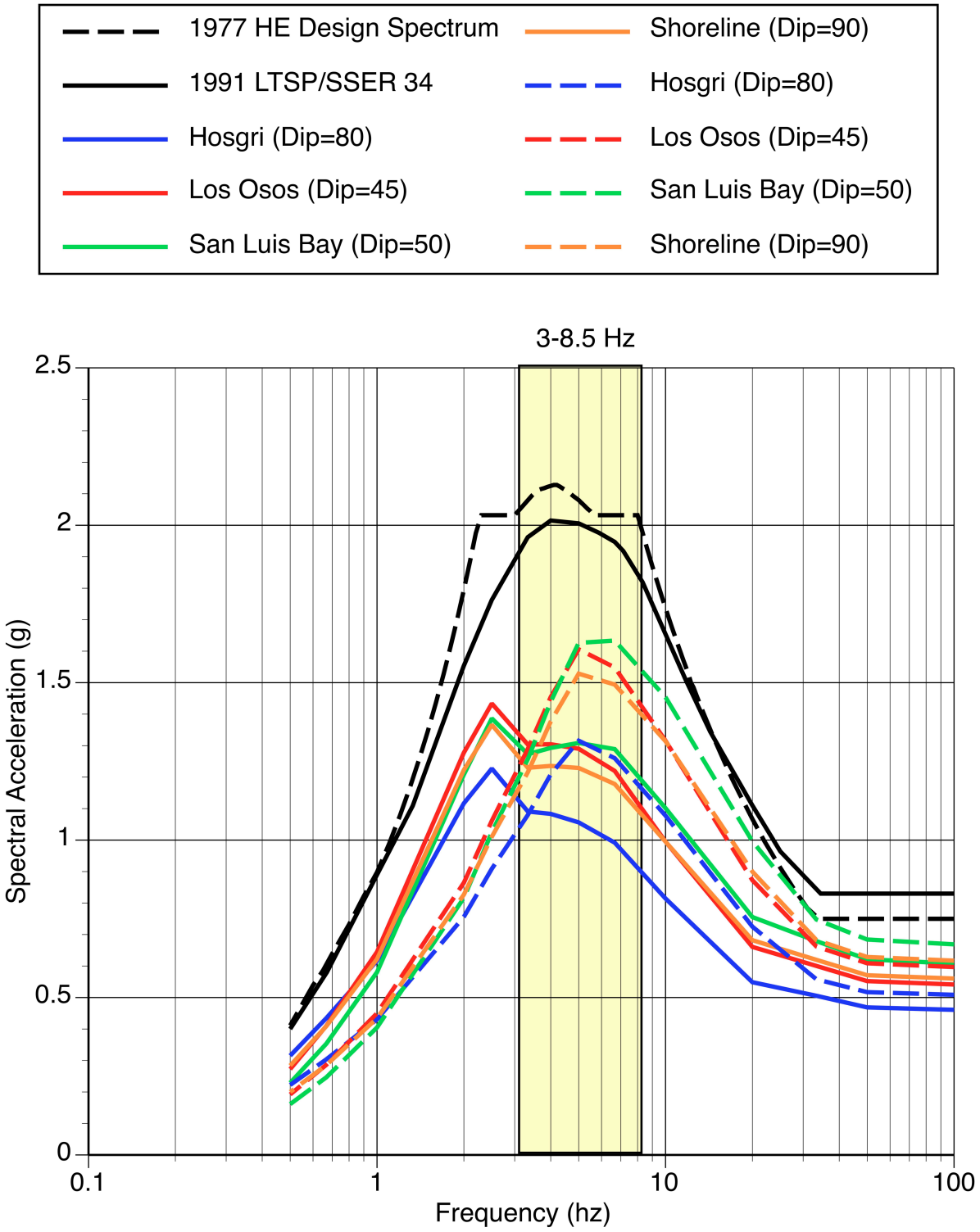

Figure 6-19. 84th percentile ground motion from the four nearby fault sources using the site-specific single-station sigma approach (solid lines) and the traditional ergodic approach (dashed lines). The 2.5 Hz peak in the site-specific spectrum reflects the DCPP site amplification.

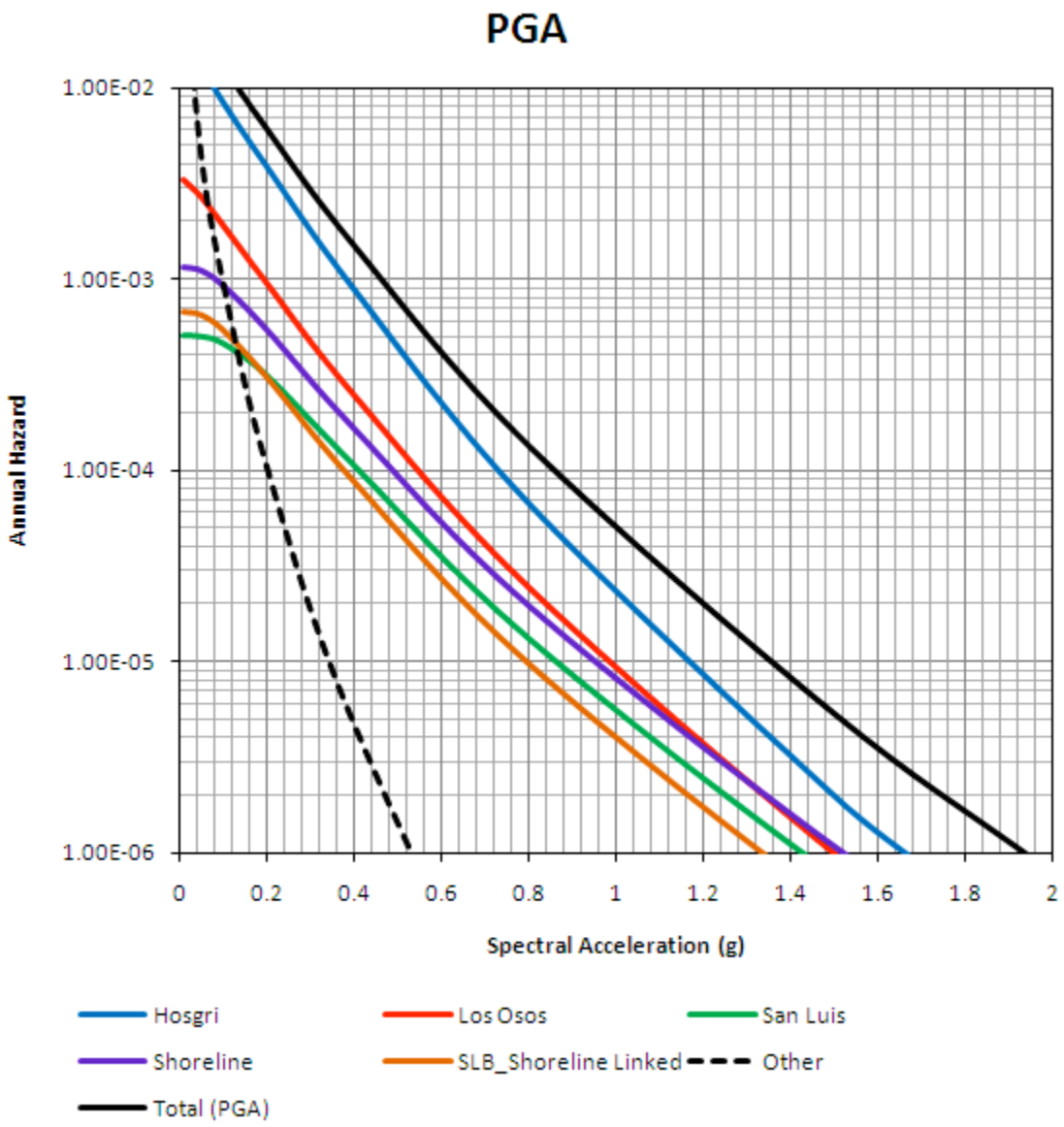

Figure 6-20a. Hazard by fault sources for PGA; the Other source includes regional sources listed on Table 6-9.

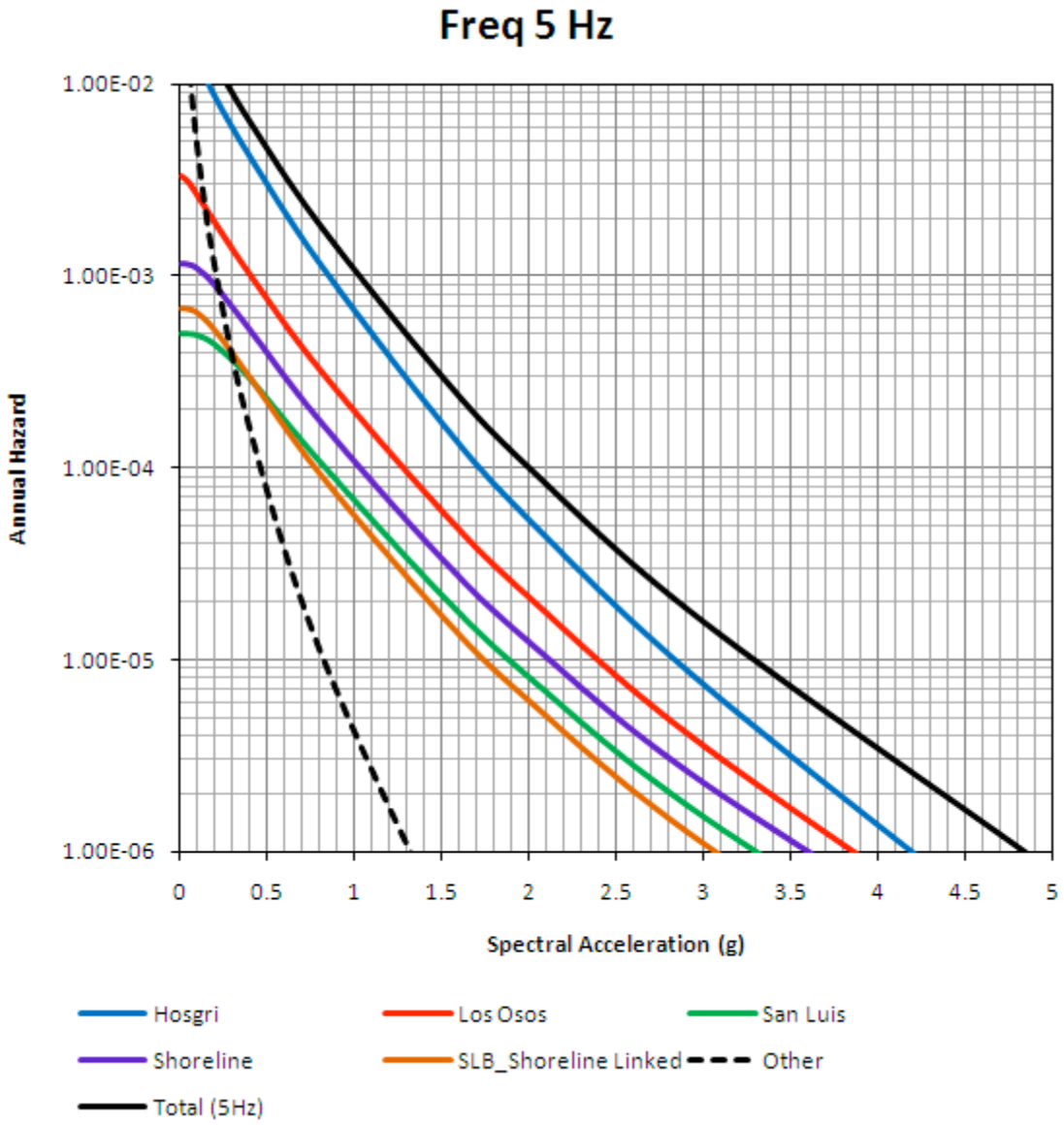

Figure 6-20b. Hazard by source for 5 Hz spectral acceleration.

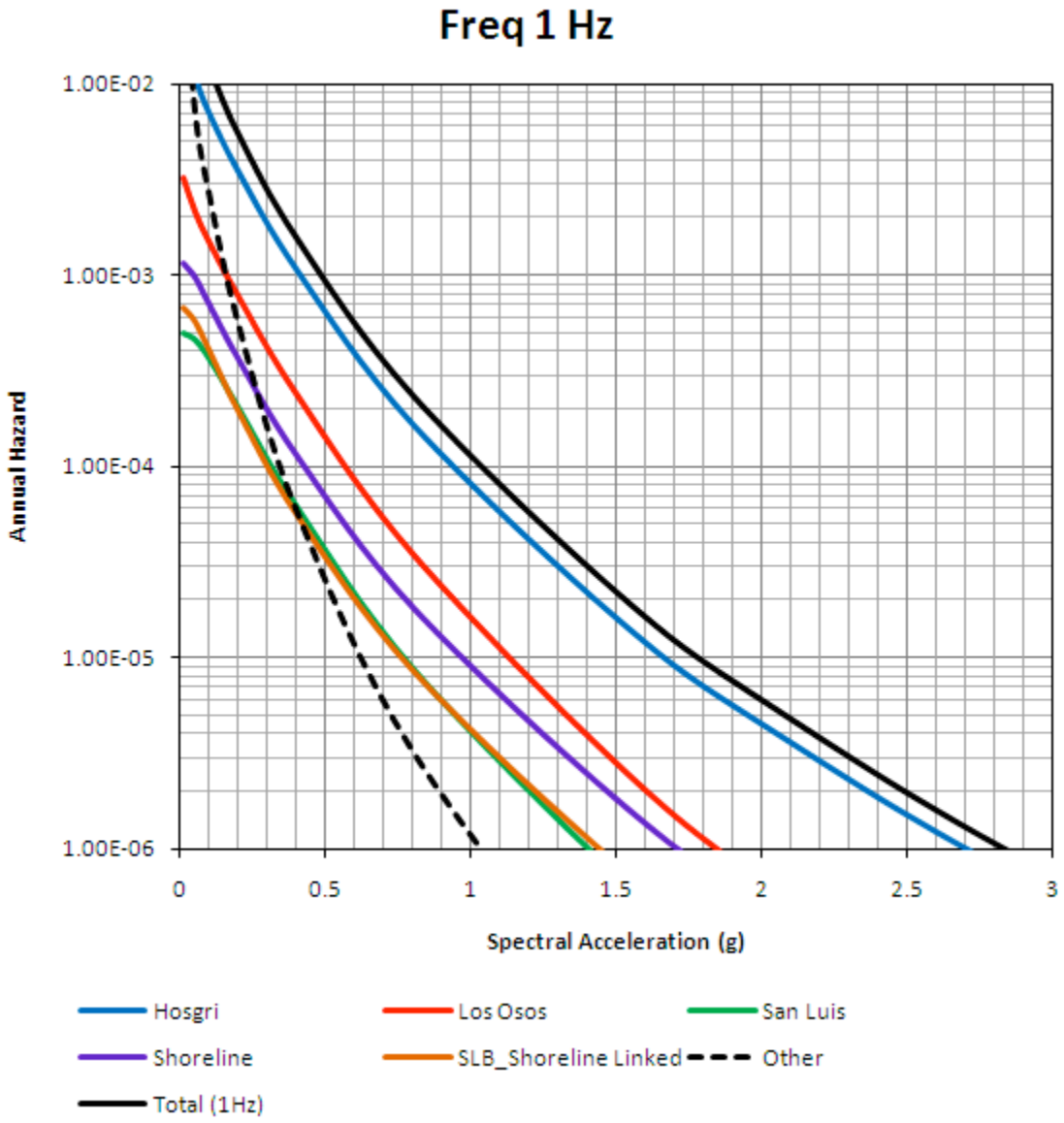

Figure 6-20c. Hazard by source for 1 Hz spectral acceleration.

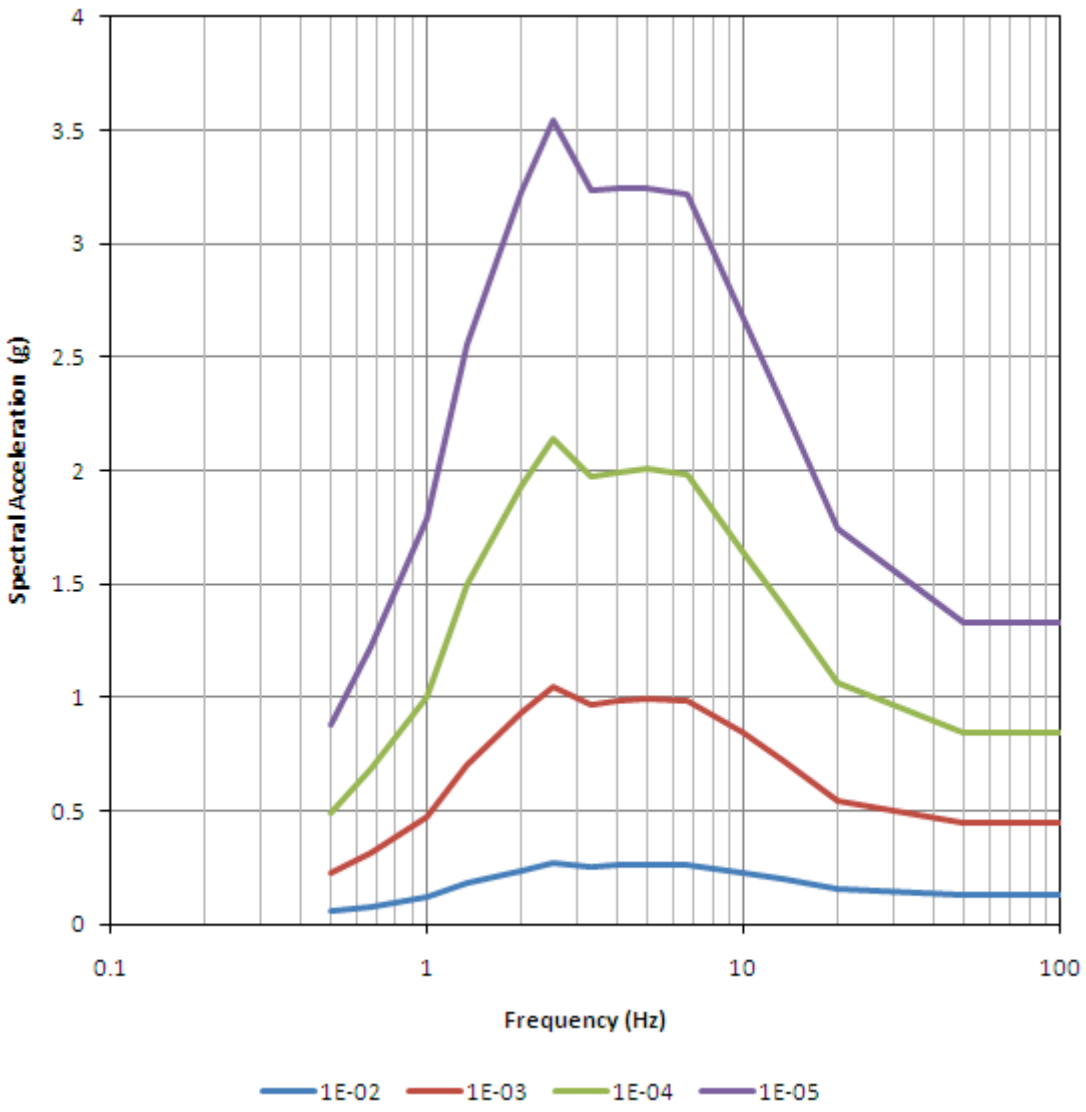

Figure 6-21. Uniform hazard spectra for four hazard levels. The peak at 2.5 Hz reflects the site-specific amplification at DCPP.

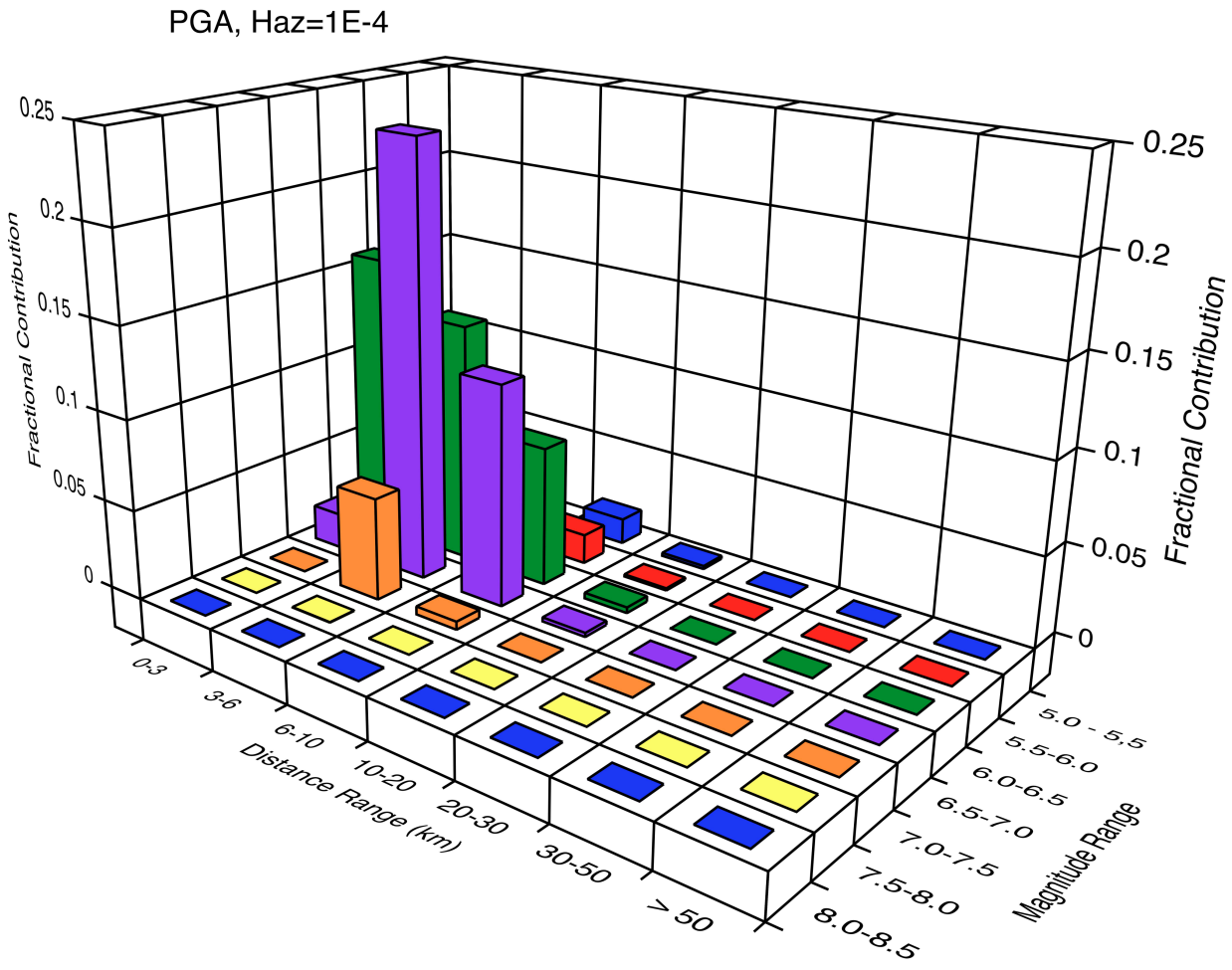

Figure 6-22a. Deaggregation for PGA for a hazard level of 1E-4.

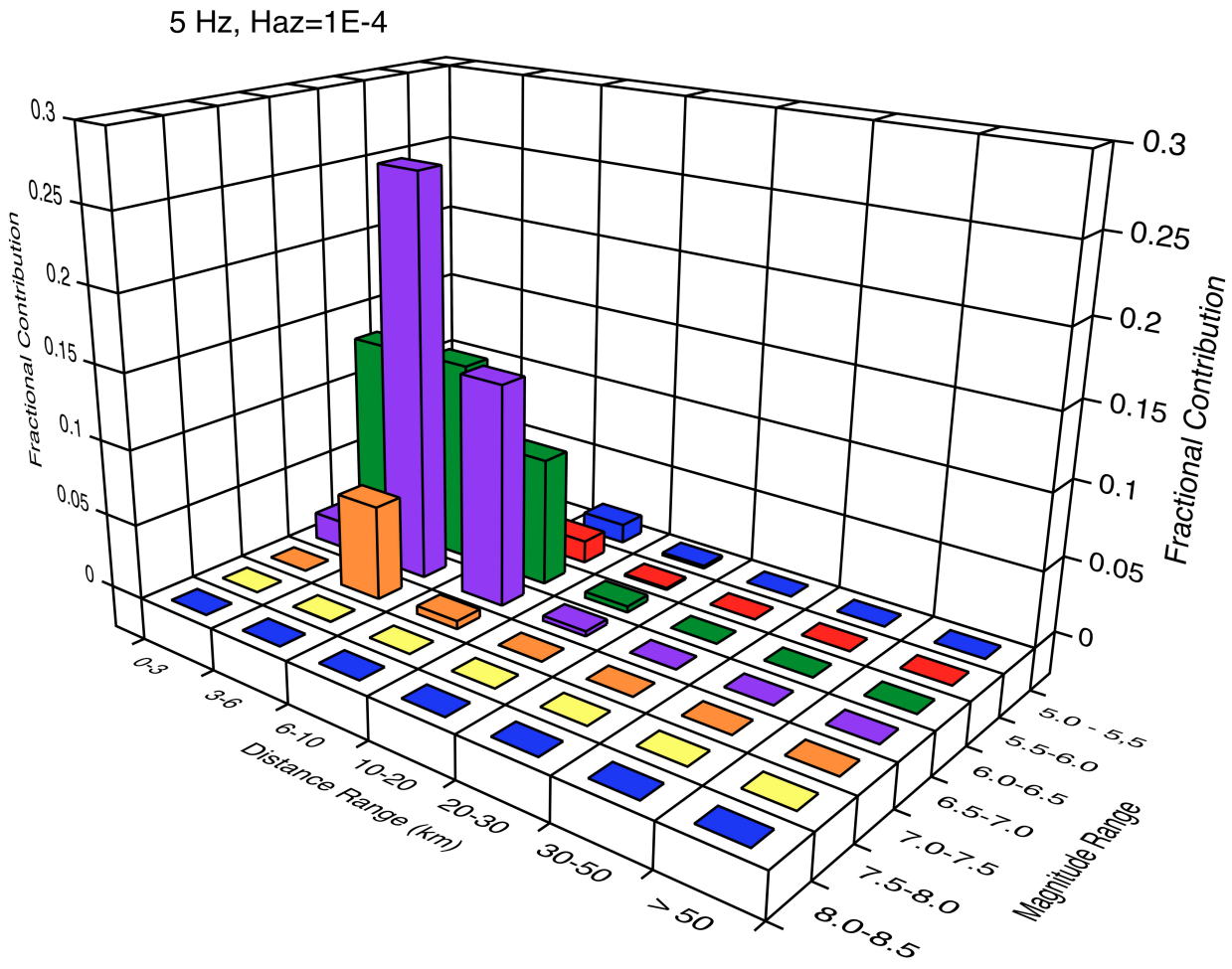

Figure 6-22b. Deaggregation for 5 Hz for a hazard level of 1E-4.

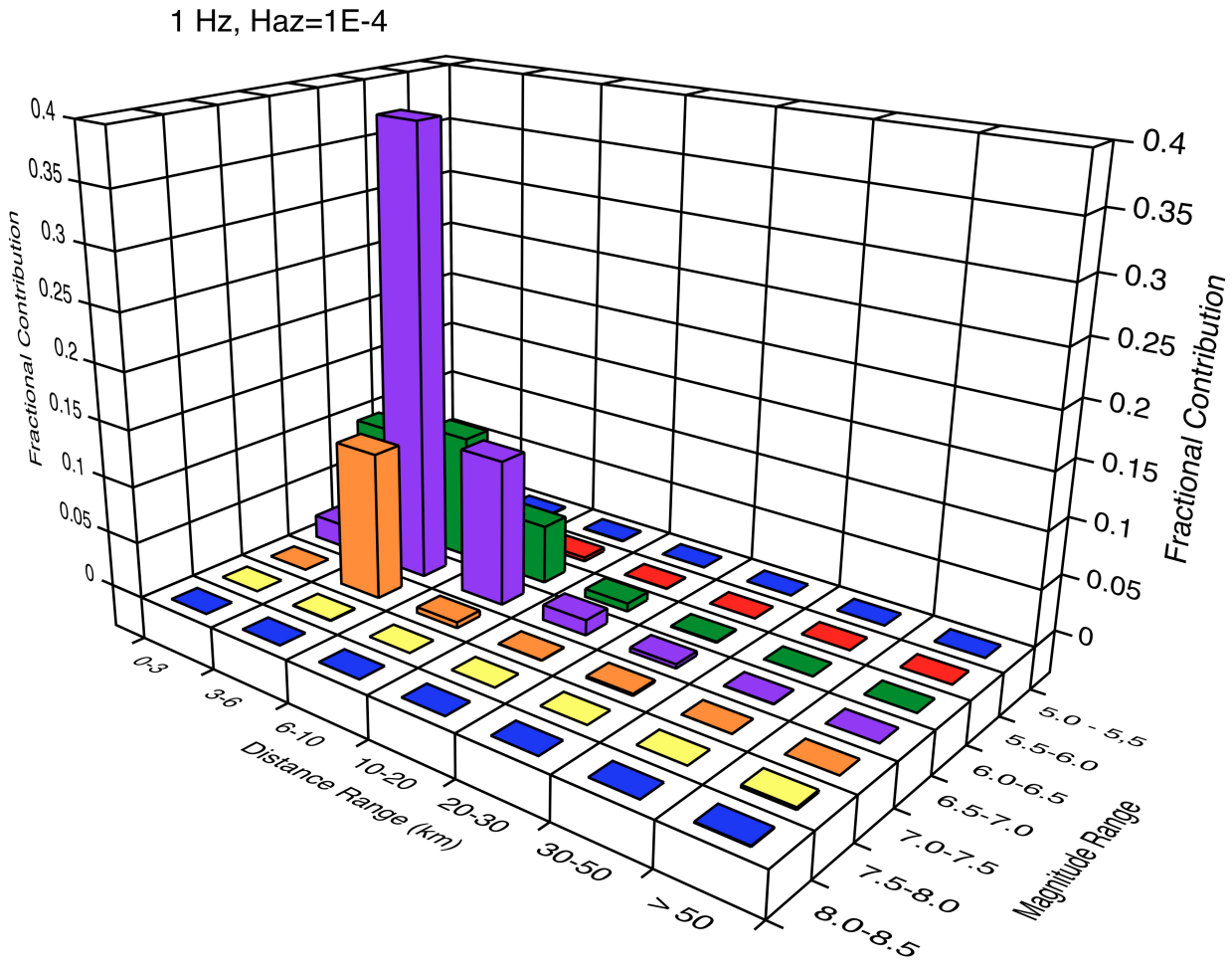

Figure 6-22c. Deaggregation for 1 Hz for a hazard level of 1E-4.

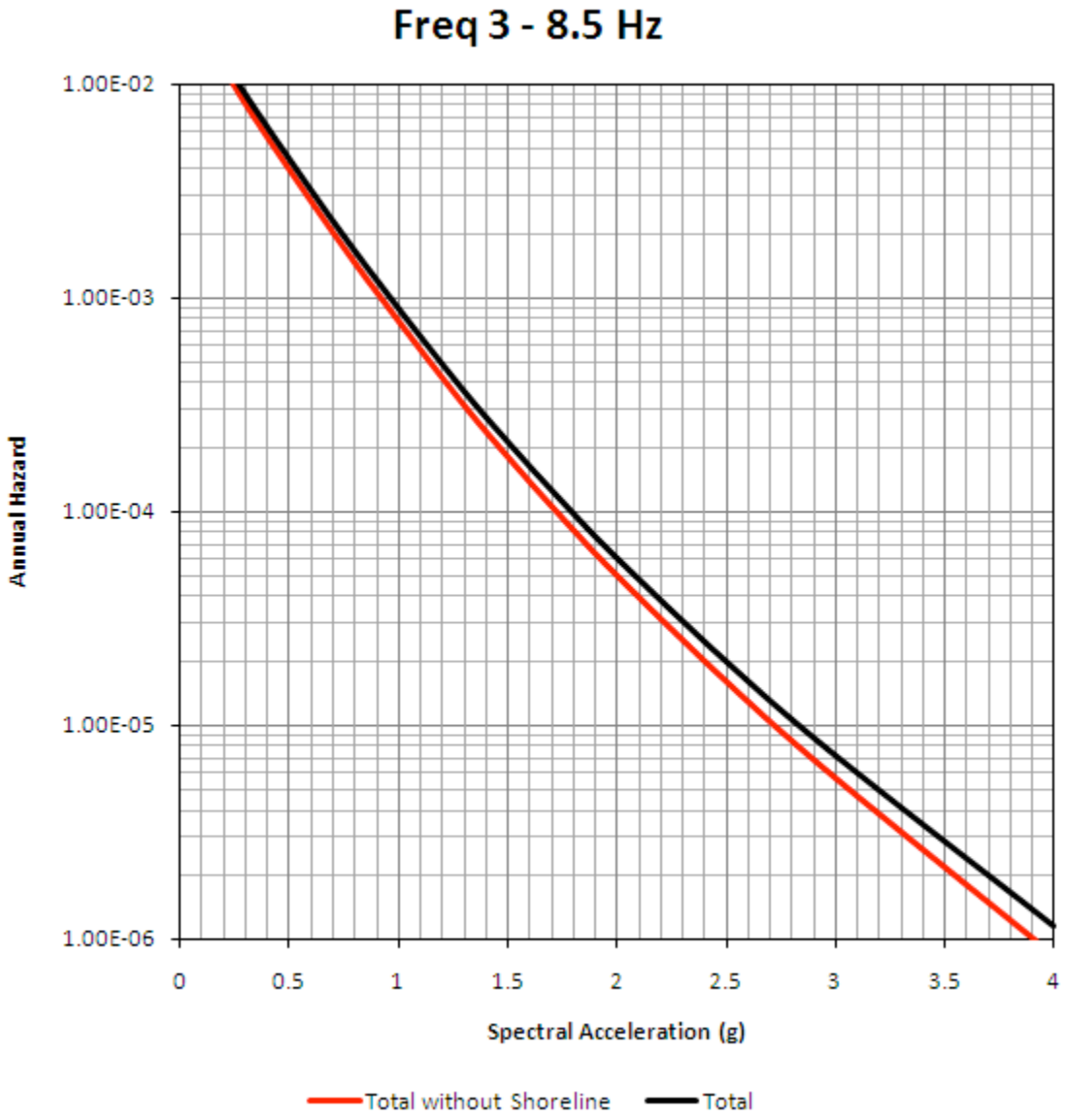

Figure 6-23. Hazard for spectral acceleration average over 3–8.5 Hz showing the contribution from the Shoreline fault source to the total hazard.

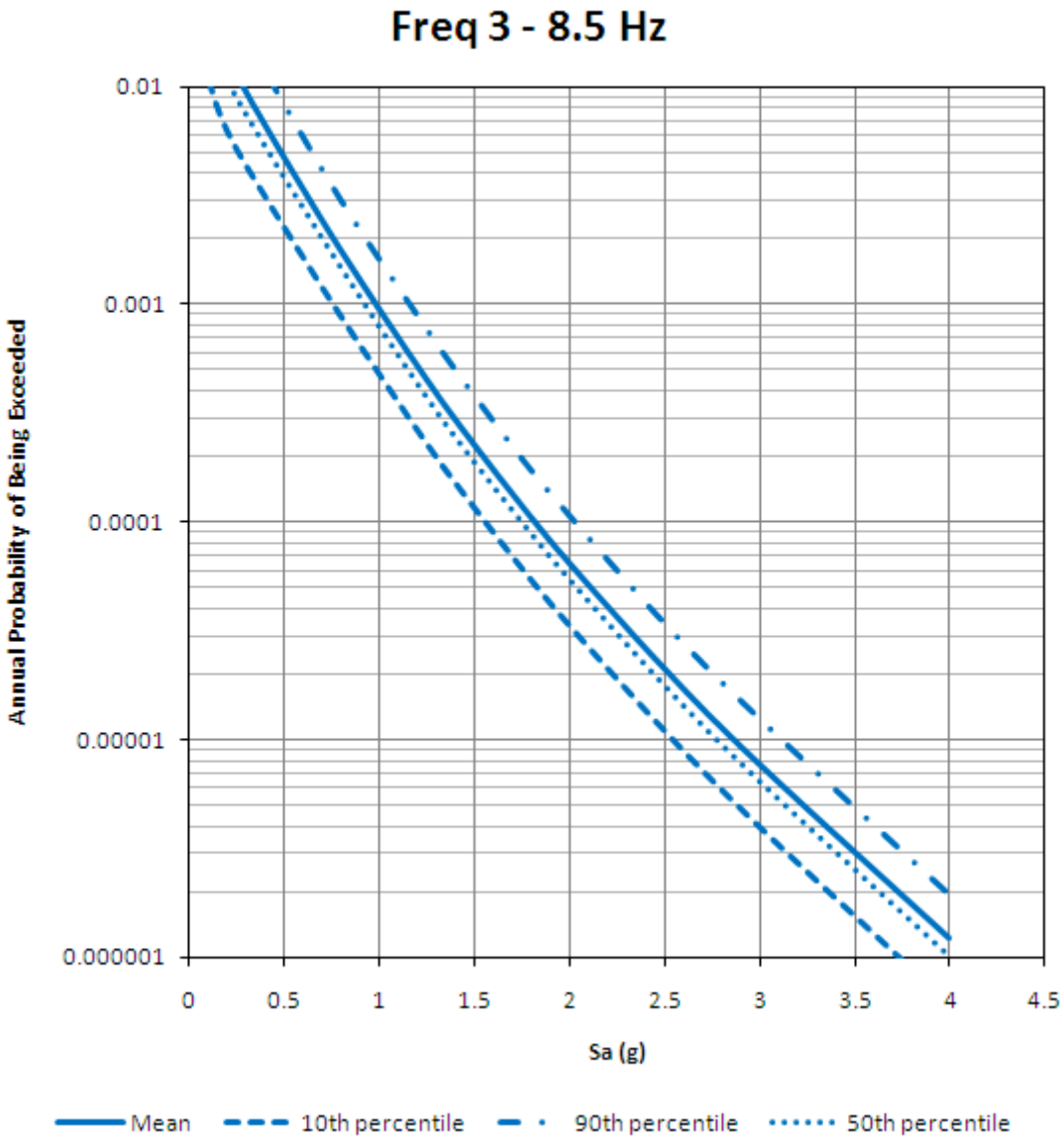

Figure 6-24. Fractiles of the hazard for 3-8.5 Hz.

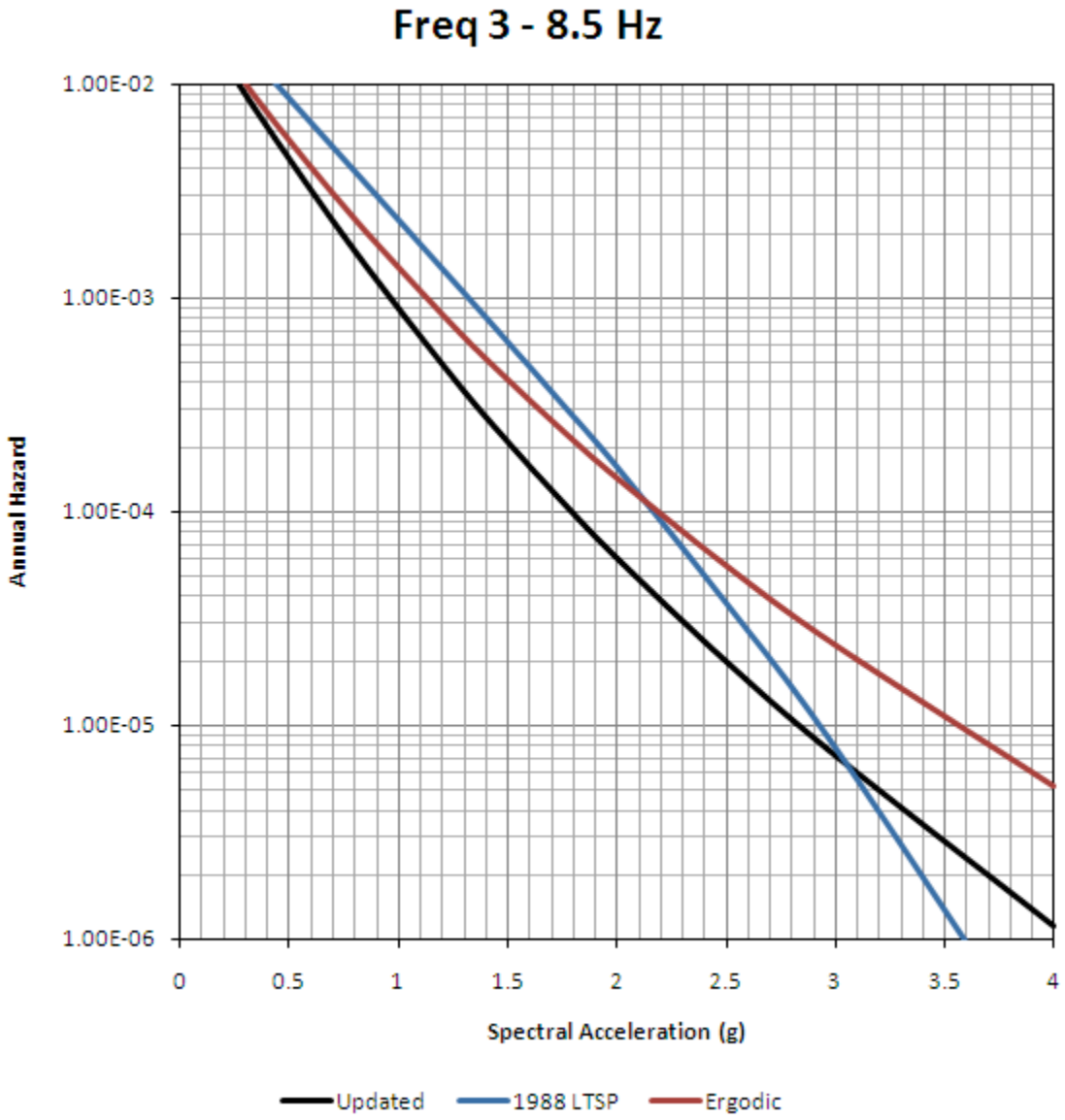

Figure 6-25. Comparison of the mean hazard for 3-8.5 Hz with the mean hazard from the 1988 LTSP (PG&E, 1988) and with the mean hazard using the traditional ergodic assumption.

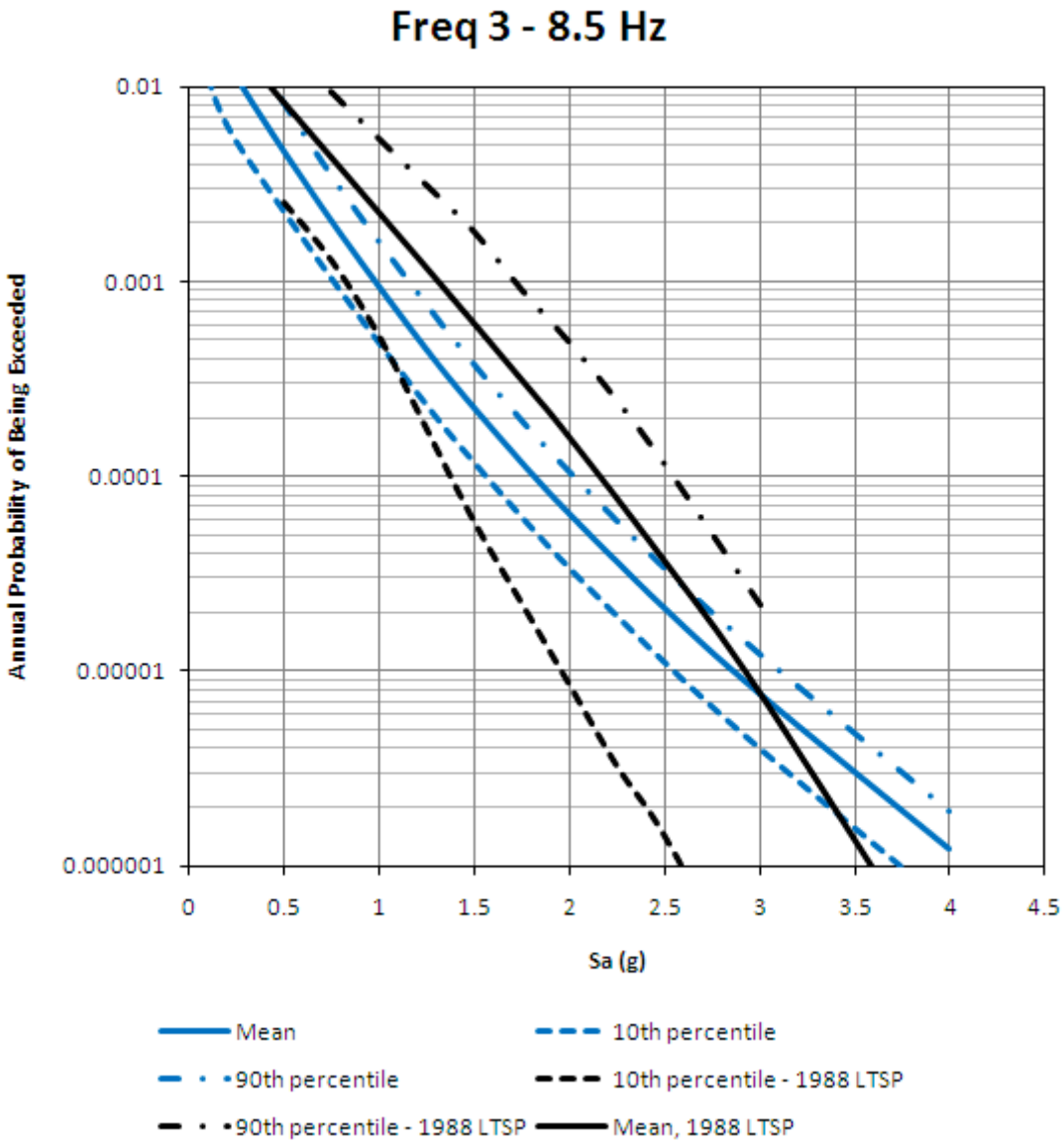

Figure 6-26. Comparison of the 3-8.5 Hz hazard fractiles from the 1988 LTSP (PG&E, 1988) (black) with the updated results (blue).